CLUSTERS ON THE EDGE: THE INTERFACE BETWEEN GALAXY CLUSTER OUTSKIRTS AND LARGE-SCALE INTERCLUSTER FILAMENTS

By

Gabriella Elan Clapper Alvarez

Dissertation

Submitted to the Faculty of the

Graduate School of Vanderbilt University

in partial fulfillment of the requirements

for the degree of

DOCTOR OF PHILOSOPHY

in

Astrophysics

May 13, 2022

Nashville, Tennessee

Approved:

Kelly Holley-Bockelmann, Ph.D.

Scott Randall, Ph.D.

Robert Scherer, Ph.D.

Christine Jones-Foreman, Ph.D.

Andreas Berlind, Ph.D.

I would like to thank Juliana Alvarez, Patrick Clapper, Dr. Heidi Morgan, and Sabrina Alvarez for their counsel and support with this thesis. I would like to thank Rodolfo Montez Jr., Nicholas Lee, Lina Pulgarin-Duque, Christine Jones-Foreman, Yuanyuan Su, and my committee members for their enlightening discussions and comments. I would especially like to thank Dr. Scott Randall for his support and mentorship, and Dr. Kelly Holley-Bockelmann for her support. I would like to thank the referees for the papers presented in this work for their helpful comments. Thank you to the Fisk-Vanderbilt Masters-to-PhD Bridge program for accepting me and standing by me.

ACKNOWLEDGMENTS

Support for GEA was partially provided by Chandra X-ray Observatory grants GO2-13161X, GO9-20118X, GO9-20112X and GO3-14133X, by the STScI grant HST-GO-15610.001, and by the Graduate Assistance in Areas of National Need (GAANN). This work received federal support from the Latino Initiatives Pool, administered by the Smithsonian Latino Center.

TABLE OF CONTENTS

LIST OF TABLES

LIST OF FIGURES

CHAPTER 1

Introduction

This chapter includes excerpts from Alvarez et al. (2018) and Alvarez et al. (2022), used with permission from the Astrophysical Journal.

1.1 Cosmic Web

Cosmological simulations of the Universe (e.g. Nelson et al., 2019; Heitmann et al., 2021), as well as cosmic microwave background (CMB) observations (e.g. Bennett et al., 2013; Planck Collaboration et al., 2016) show that the matter content of the early Universe was relatively homogeneously distributed throughout space with small temperature and density perturbations (see e.g. Figure 1.1).

As the Universe has evolved through time, the matter condensed further and further, as dictated by the density perturbations in the infant Universe. The peaks in density in the early universe grew into the nodes of a web-like structure of cosmological filaments (see e.g. Figure 1.2). Groups of galaxies formed through the merging of individual galaxies, and subsequently these groups of galaxies merge to form clusters of galaxies, or the nodes (e.g. Kauffmann et al., 1999). This hierarchical cluster formation is thought to happen along and at the nodes of the cosmic filaments that comprise the large-scale structure of the Universe.

1.2 Nodes–Galaxy Clusters

Clusters of galaxies are the largest known bound objects in the Universe. Massive galaxy clusters, comprised of 100s to 1000s of galaxies bound to each other by gravity, in the local Universe, were first catalogued

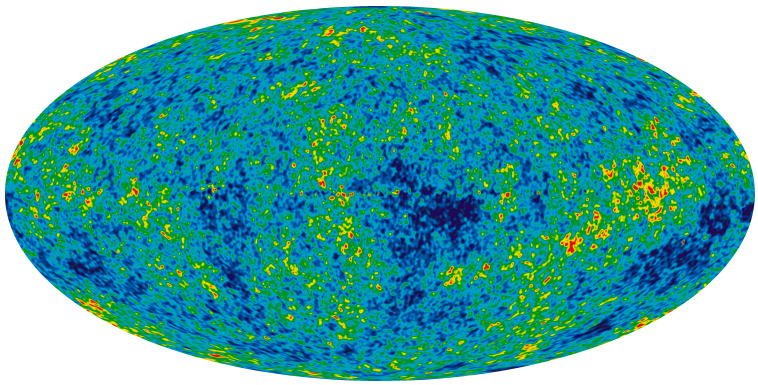

Figure 1.1: All-sky image of the early Universe (Bennett et al., 2013), $\sim$ 13.77 Gyr ago, in the microwave band. The temperature fluctuations are indicated by the color scale, and are theorized to have grown into the nodes of the large-scale structure of our Universe. The image shows a temperature range of $\pm 200 \mu$K.

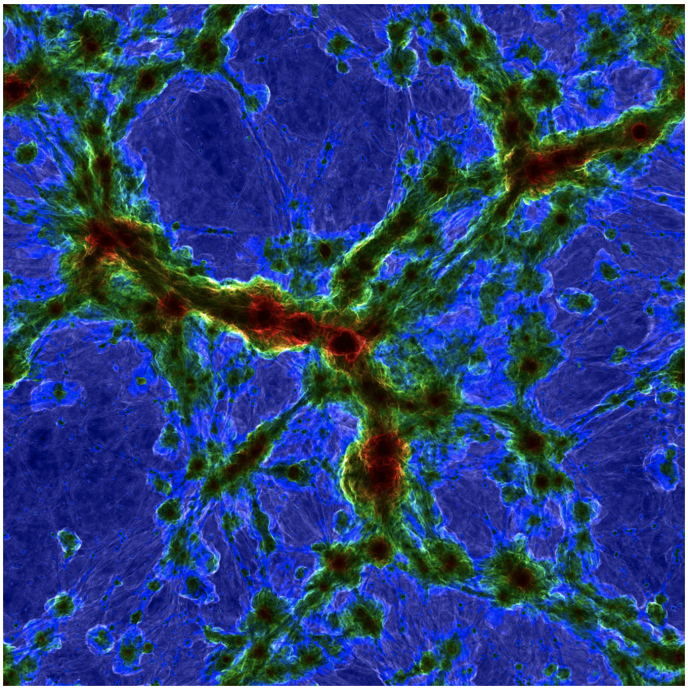

Figure 1.2: A snapshot from the IllustrisTNG100 (Nelson et al., 2019) cosmological simulation. Color indicates gas temperature, where cooler gas is bluer and hotter gas is redder. Red indicates 10^7 K gas near the centers of the simulated galaxy clusters. The brightness scale is dictated by shock strength. The bright structure shows accretion shocks at the boundaries of galaxy cluster outskirts and cosmic filaments.

optically by Abell (1957). There have been a multitude studies since then of galaxy clusters across the electromagnetic spectrum (e.g. as decrements in the CMB (Sunyaev and Zeldovich, 1970, 1980)).

It is found that most of the gas mass in galaxy clusters lies in the intracluster medium (ICM), which is a hot ionized plasma ($T \sim 10^7$ K) that permeates the entire cluster. The ICM is X-ray bright (e.g. Markevitch and Vikhlinin, 2007) due to Bremmsstrahlung, or breaking, radiation from the diffuse plasma. Since the surface brightness of such radiation is proportional to the square of the gas density, the central regions of galaxy clusters, where the ICM is densest, have been very well studied due to the superior angular resolution of i.e. *Chandra* and XMM-*Newton* compared to cluster outskirts ($r > r_{500}$[1]).

1.2.1 Cluster Cosmology

Since the formation and evolution of galaxy clusters are so closely tied to the density perturbations of the early Universe, they have the potential to be very powerful tools towards better understanding cosmology and the growth and evolution of larger-scale structure of the Universe through time.

To investigate cosmological parameters in a quantifiable manner using galaxy clusters, the evolving cluster mass function is employed (i.e. Ikebe et al., 2002; Schellenberger and Reiprich, 2017), usually in conjunc-

[1] r_Δ is the radius of a sphere whose mean matter density is Δ times the critical density of the universe

tion with other independent tools, such as the primary anisotropies in the CMB, in order to break degeneracies between cosmological parameters. This function is particularly sensitive to the cosmological parameters for normalized mass density Ω_M and spatial variance σ_8.

While there are many methods employed to explore the cosmological parameter space, it is important to understand systematic errors that may skew or bias results.

When using X-ray observables, many assumptions must be made when estimating the mass of the cluster. One method is to assume that the ICM, a direct observable in the X-ray regime, is comprised of a sphere in hydrostatic equilibrium. Another mass estimation method using X-ray data is to employ scaling relations, such as the Luminosity-Temperature relation (i.e. Giodini et al., 2013) as a proxy for the total mass of the cluster. Other mass estimation methods, such as weak graviational lensing, may be used to calibrate these scaling relations. However, even this method is subject to its own known and unknown biases such as noise bias (Massey et al., 2013), asymmetry of the point spread function (Hirata and Seljak, 2003), mass sheet degeneracy (Schneider and Seitz, 1995), and incorrect photometric redshifts and miscentering (Köhlinger et al., 2015).

1.2.2 Galaxy Cluster Outskirts

Galaxy cluster outskirts are defined as $r_{500} \sim r_{200}$ [2] in this work due to the limitations of the X-ray instruments employed.

Figure 1.3, a simulation of a galaxy cluster, highlights the fact that galaxy cluster outskirts vary in both surface brightness and temperature azimuthally, especially where they interface with filaments. As stated in the previous section, a key assumption when using galaxy clusters for precision cosmology is that clusters are in hydrostatic equilibrium.

Dark matter only simulations show that galaxy clusters evolve in a self-similar manner (Voit et al., 2005). However, it has been observed that many massive galaxy clusters seemingly deviate from hydrostatic equilibrium at large cluster radii (e.g. Walker et al. (2013)). Another key assumption is the geometry of the cluster, nominally a sphere. Rather the "splashback radius" (R_{sp}), which is not spherically symmetric, better defines the cluster outskirt boundaries. However, this radius remains difficult to ascertain with observational data. Additionally, as can be shown in (i.e. Schellenberger et al., 2015), instrumental callibrations, and therefore systematic errors, are still relatively unknown in the X-ray regime, further biasing mass estimates.

The deviation of hydrostatic equilibrium at large cluster radii could be due to a number of physical processes in the ICM, including clumping of cool gas (Eckert et al., 2015; Simionescu et al., 2011; Tchernin et al., 2016) at large cluster radii ($\sim r_{200}$) biasing the average surface brightness of cluster outskirts high;

[2] r_Δ is the radius at which the mean cluster density is Δ times the critical density of the universe at the redshift of the clusters

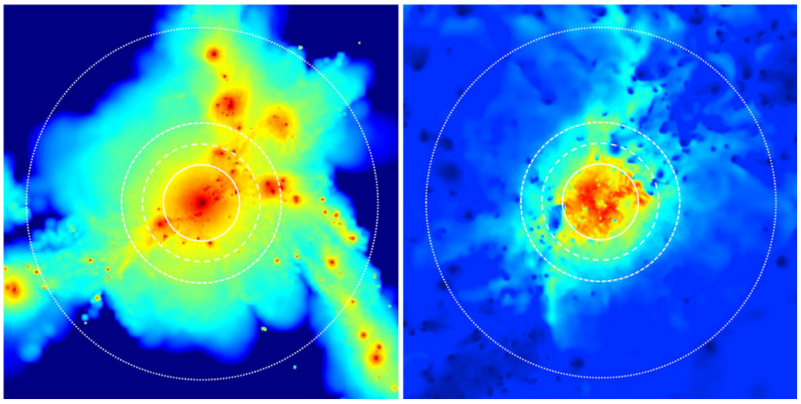

Figure 1.3: Simulated galaxy cluster with the white lines from the inside out being r_{500}, r_{200}, r_{vir}, and $3r_{200}$. Left: The X-ray surface brightness in the 0.5-2.0 keV band. Right: Linear scale temperature map from 0-11 keV and the color bar is respectively blue to red. Figure taken from (Reiprich et al., 2021).

non-thermal pressure support from bulk motions, turbulence or cosmic rays (Lau et al., 2009; Vazza et al., 2009; Battaglia et al., 2013); and electron-ion non-equilibrium (Fox and Loeb, 1997; Wong and Sarazin, 2009; Hoshino et al., 2010; Avestruz et al., 2015).

The ICM thermodynamic history of clusters is encoded in the entropy profiles of the ICM. Unlike larger mass clusters, the few studies of lower mass galaxy clusters and groups with the X-ray telescope *Suzaku* have shown close agreement in the virialization region between the predicted entropy profiles based on self-similar gravitational collapse models, and the inferred entropy profiles of the systems based on X-ray spectroscopy studies (Su et al., 2015; Bulbul et al., 2016; Sarkar et al., 2021). This could be due to the fact that galaxy groups are likely more evolved than galaxy clusters (Paul et al., 2017).

Another theory is that due to their smaller mass, galaxy groups are more sensitive to common thermodynamic processes such as stellar and active galactic nuclei (AGN) feedback (e.g. Pratt et al., 2010; Lovisari et al., 2015), injecting entropy into their outskirts. This injected entropy could artificially correct for the entropy deficiency observed in more massive clusters around the virialization region, making the ICM of the lower mass cluster or group look like it's obeying self-similarity. However, an entropy excess at large group and low mass cluster radii has not yet been observed. Isolated groups also tend to be in less dynamically active regions than clusters, as they are not at the nodes of the cosmic web. The relative isolation would lead there to be fewer clumps, weaker accretion shocks, and less turbulence.

Simulations (e.g. Angelinelli et al., 2021) and deep X-ray observations (e.g. Mirakhor and Walker, 2020) of galaxy clusters have revealed that the thermodynamic structure of the outskirts varies azimuthally, presumably due in large part to the growth of hierarchical structure through cosmic filaments. Understanding the physical processes at work in the ICM in the outskirts of clusters is key to our understanding of the growth of

cosmic structure, and using clusters for precision cosmology.

This work seeks to further investigate the outskirts of galaxy clusters, particularly where they interface with large-scale intercluster and cosmological filaments in order to characterize and explore these deviations from hydrostatic equilibrium.

1.3 Missing Baryons and the WHIM

Theory and observations both suggest that there are fewer baryons detected in the local universe than predicted. Observations of the cosmic microwave background (i.e. Planck Collaboration et al., 2015) and Big Bang nucleosynthesis (BBN) models (Kaplinghat and Turner, 2001) predict that baryons comprise approximately 5% of the total mass budget in the Universe. In the local universe, the known baryon content falls short by approximately a factor of two (Fukugita et al., 1998; Cen and Ostriker, 1999; Bregman, 2007; Sinha and Holley-Bockelmann, 2010). This discrepancy is known as the "missing baryons problem."

It is theorized (e.g. Cen and Ostriker, 1999; Davé et al., 2001)) that the bulk of these missing baryons may be in the form of a diffuse gas that traces the filaments of the cosmic web, known as the warm-hot intergalactic medium (WHIM). Simulations predict WHIM temperatures of $\log \frac{\mathrm{T}}{\mathrm{K}} \simeq 5-7$ and electron densities of $n_e \simeq 10^{-7}-10^{-5}$ cm^{-3} (see Bregman, 2007), making this medium very difficult to observe directly with most existing observatories. Tentative evidence has been found for the WHIM in the form of absorption lines in the soft X-ray spectra of high redshift objects (e.g. Zappacosta et al., 2012; Nicastro et al., 2018). However, observations via absorption lines have been unable to constrain the amount of baryons present or to trace large-scale filamentary structure.

There has yet to be a high significance observation of the WHIM in large-scale filaments (i.e. Kull and Böhringer, 1999; Fang et al., 2007) aside from a handful of possible detections of the more dense part of the WHIM at the outskirts of galaxy clusters (Wang et al., 1997; Werner et al., 2008; Eckert et al., 2015; Bulbul et al., 2016). More recently, de Graaff et al. (2017) claimed a 5.1σ detection of WHIM filaments using stacked Sunyaev Zel'dovich measurements. Nicastro et al. (2018) claimed a $\sim 4\sigma$ detection of the WHIM using X-ray absorption spectra with XMM-*Newton*.

Galaxy clusters are excellent probes of the large-scale distribution of the WHIM, because they are found at the intersection of dark matter filaments (i.e. González and Padilla, 2009). This makes galaxy clusters excellent probes to study large-scale and intercluster filaments. The WHIM may have an impact on the ICM of galaxy clusters, particularly where the ICM in the outskirts of the clusters are expected to interface with the WHIM in large-scale filaments. Entropy profiles of the ICM are generally found to lie below what one would expect based on pure gravitational collapse models (Kaiser, 1986; Voit et al., 2005) near a cluster's virial radius (i.e. Edge and Stewart, 1991; David et al., 1995; Allen and Fabian, 1998; Arnaud and Evrard,

1999; Walker et al., 2013; Urban et al., 2014). This interaction triggers thermodynamic processes, causing departures from the expected hydrostatic equilibrium (i.e. Ichikawa et al., 2013).

This work additionally seeks to search for the WHIM as a possible solution to the missing baryon problem. The objects for this study are carefully chosen based upon their merging state and configuration in the sky. Since the WHIM is theorized to have a relatively low surface brightness, galaxy clusters that are in the early stages of merging are chosen for this study. In pre-mergers, the merger axis is purportedly aligned with the local cosmic filament, and the clusters may not be aligned after core passage if there is a non-zero impact parameter. This gives us an a priori expectation of where the WHIM filaments should be. As stated in Section 1.1, galaxy clusters form hierarchically through merging along and at the node of cosmological filaments, therefore the merging clusters are presumably within or connected by the filaments and indicate the presence of larger-scale structure. Additionally, if these major merging systems are inclined to the line of sight, the projected surface brightness of the intercluster filament would make this bridge appear brighter than if the system is oriented in the plane of the sky.

CHAPTER 2

Objects of Study

This chapter includes excerpts and figures from Alvarez et al. (2018) and Alvarez et al. (2022), used with permission from the Astrophysical Journal.

This section will motivate why the objects were chosen for the study of this thesis.

2.1 Abell 3391/Abell 3395

The double X-ray peaked cluster Abell 3395 (hereafter A3395) was first characterized with Einstein observations (Forman et al., 1981), and comprises of A3395NW and A3395SE. These two clusters are currently undergoing a major merger and share a filament of visible ICM material to the north of both cluster centers (see e.g. Figure 3.1 Right). A3395 is relatively close in both projected separation on the sky and redshift, to Abell 3391 (hereafter A3391). There is a galaxy group, ESO 161-IG 006 (hereafter ESO-161) located between the two subclusters, in the intercluster filament, in alignment with the clusters. In Table 3.1 shows the cluster masses (Piffaretti et al., 2011) and group mass estimated in this work, redshifts for the group and clusters (Tritton, 1972; Santos et al., 2010), positions[1], r_{500} (Piffaretti et al., 2011), and their X-ray temperatures (Vikhlinin et al., 2009). The cluster centers have a separation of $47.08'$ on the sky, which corresponds to 2.9 Mpc at their mean redshift.

Figure 2.1 shows the velocity information from individual galaxies in this system to illustrate that either there are two halos at slightly different redshifts with halos overlapping each other in projection, or a connected system that inclined along the line of sight. Tittley and Henriksen (2001) performed a dynamical analysis of the A3391/A3395 system and found that it is likely inclined close to the line of sight ($3.1^\circ - 9^\circ$). This finding made the A3391/A3395 system a prime candidate to further investigate with the next generation of X-ray telescopes, as the projected emission along the filamentary region would have a higher surface brightness than if the system was inclined to the plane of the sky.

ROSAT ASCA observations were the first to reveal that this system has excess material in the intercluster filamentary region between A3391 and A3395 (Tittley and Henriksen, 2001). Tittley and Henriksen (2001) performed a ray tracing simulation on two images to account for the scattering of light into the region of the apparent filament. One image includes the intercluster filamentary region and the other image has this region "blanked" out (panel a and b respectively in Figure 2.2). The "blanked" image is set to have a constant count

[1]The NASA/IPAC Extragalactic Database (NED) is operated by the Jet Propulsion Laboratory, California Institute of Technology, under contract with the National Aeronautics and Space Administration.

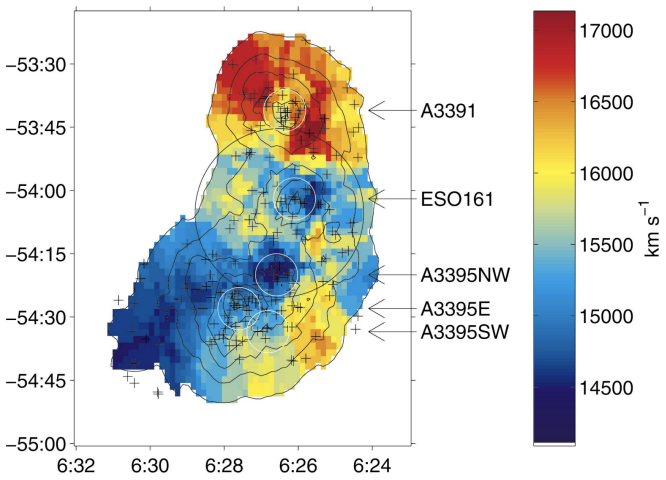

Figure 2.1: The galaxy concentration and mean redshifts of the A3391/A3395 system. The crosses indicate where the galaxy sample is. The mean local density of the galaxies is indicated by the contour levels, which are separated by factors of 2. The mean local radial velocity is illustrated by the color scale. Redshift data outside the coutors should be ignored. The white circles ($r = 5'$) indicate A3391, ESO-161, A3395NW, and A3395SE from north to south. The larger dark circle is the *ROSAT ASCA* GIS field of view. Figure taken from Tittley and Henriksen (2001).

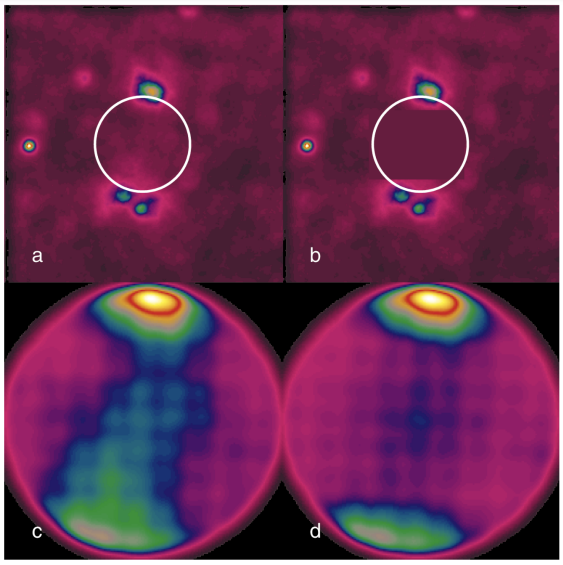

Figure 2.2: The distribution of light, including scatter, estimated to be measured at the image plane of the GIS detector by image ray-tracing. As input, *ROSAT* All-Sky Survey data (top row) were used. The ray-tracing was done by the tool *trace–asca*. Image a was traced to produce image c. Image b had the intercluster field "blanked", which was subsequently ray-traced to produce image d. Figures and caption taken from Tittley and Henriksen (2001).

rate that matches at a similar radius in a direction that is off the filament axis. Panel c has a significant amount of flux to the north of A3395 that is absent in panel d of Figure 2.2, thus indicating that the emission seen in the filamentary region is physical in origin and not the result of scattered light.

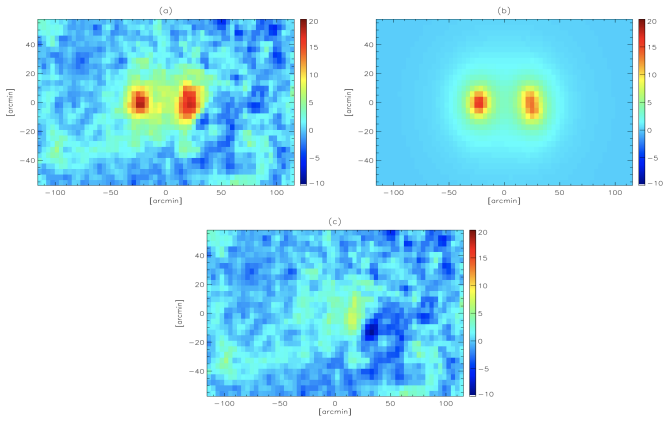

Figure 2.3: a) tSZ Compton parameter map ($y \times 10^6$), b) best-fit model of the clusters, and c) residuals after subtracting the best fit model for the A3391 and A3395 pair of clusters. Figure and caption taken from Planck Collaboration et al. (2013).

Figure 2.3 a shows the *Planck* tSZ observation of the A3391/A3395 system rotated $\sim 90°$, panel b shows the best fit generalized Navarro Frenk and White (GNFW) model, and panel c shows the residual image after subtracting the image in panel b from the image in panel a. The residual image shows a clear excess in the intercluster filamentary region with a Compton y-parameter of $Y = (4.5 \pm 0.7)10^{-3}$ (Planck Collaboration et al., 2013). The authors found that the excess emission was suspiciously close to the region to the north of A3395 where the subclusters are sharing ICM material. Further analysis with higher angular resolution instrumentation is required to confirm the SZ detection of the filament.

Sugawara et al. (2017) found with *Suzaku* observations of A3395 and part of the intercluster filamentary region (see Figure 2.4), that there is evidence of ICM heating in the intercluster region above what is expected from the universal temperature profile for the system. The authors attribute this ICM heating to a possible early-stage merger shock between A3395 and A3391.

This system is a prime candidate to investigate the interface between cluster outskirts and larger-scale structure, in this case an intercluster filament, for many reasons. As stated earlier, the filament orientation ($3.1° - 9°$ along the line of sight) is favorable in the sense that the projected ICM surface brightness is higher than if the system was aligned to the plane of the sky, allowing X-ray analysis of this diffuse emission to attain a higher signal to noise. Previous studies have shown that there is excess emission between the two subclusters that can possibly be attributed to an intercluster filament (Tittley and Henriksen, 2001; Planck Collaboration et al., 2013; Sugawara et al., 2017). If these subclusters are indeed in the early stages of merging along a larger-scale filament, or cosmic filament, the cooler WHIM gas could be present and detectable in this bright region.

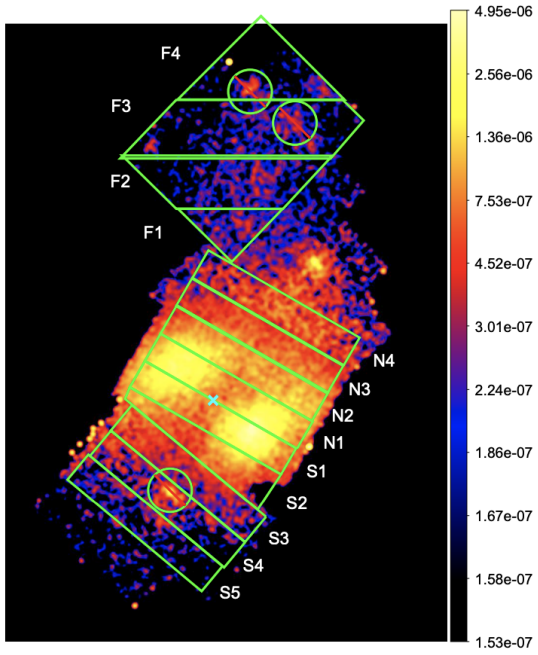

Figure 2.4: A *Suzaku* XIS3, NXB subtracted, exposure corrected, image of A3395 and the filamentary region in the 0.5-8.0 keV band. The image is smoothed by a $0.26'$ Gaussian kernel width. Green circles are excluded point source regions. Figure taken from Sugawara et al. (2017).

2.2 Abell 98

Abell 98 consists of three subclusters (Abell et al., 1989); Abell 98N (A98N), Abell 98S (A98S), and Abell 98SS (A98SS) distributed colinearly in projection (see e.g. Figure 2.5).

The right ascension and declination (Jones and Forman, 1999; Burns et al., 1994), redshift (White et al., 1997; Pinkney et al., 2000), and measured electron temperature and inferred r_{500} (Vikhlinin et al., 2009) are presented in Table 3.2.

The bimodal distribution of A98N and A98S was first seen in the X-ray with the *Einstein* telescope (Forman et al., 1981; Henry et al., 1981). A98SS was also later observed with the *Einstein* telescope (Jones and Forman, 1999). The presence of three subclusters aligned colinearly on Mpc scales suggests the presence of a local large scale structure filament aligned with the subclusters. The inference that the subclusters are connected by intercluster filaments, and are part of a larger-scale cosmic filament, makes the A98 system an ideal candidate for this study.

Paterno-Mahler et al. (2014) found, with relatively shallow *Chandra* and XMM-*Newton* observations, that there is marginal evidence for a shock heated region to the south of A98N (see Figure 2.7), perhaps due to an early stage cluster merger. Their dynamical analysis supported this conclusion. This study also determined that A98S has an asymmetric ICM distribution, indicating that A98S is still undergoing a major merger.

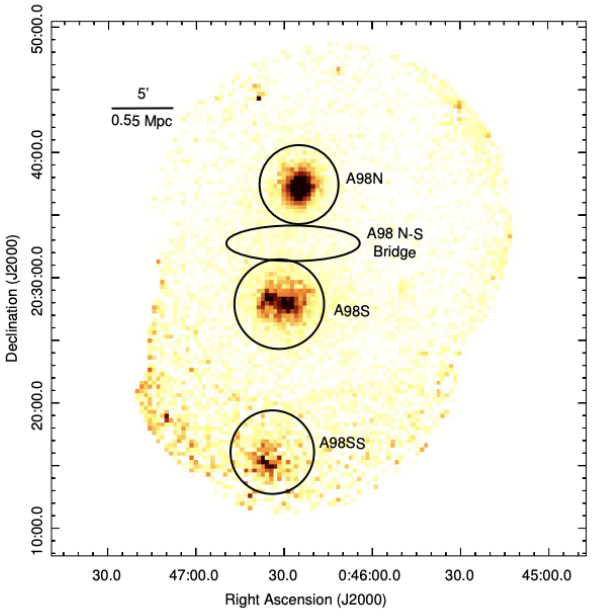

Figure 2.5: Exposure and background corrected XMM-*Newton* EPIC image of the A98 system in the 0.4–10.0 keV energy band. Figure taken from Paterno-Mahler et al. (2014).

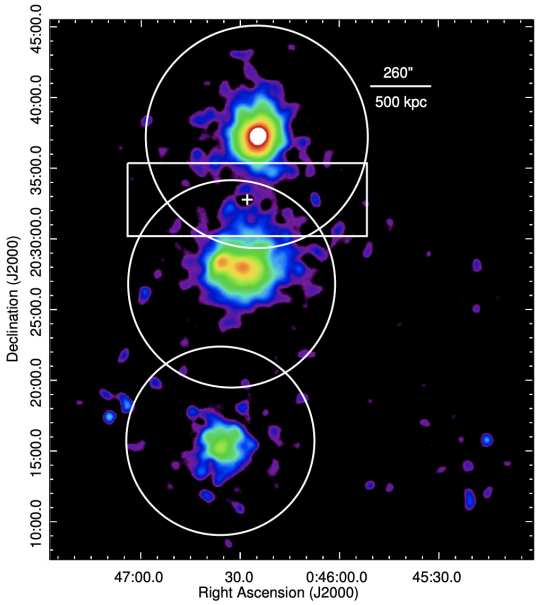

Figure 2.6: *Chandra* mosaic image binned by 4 pixels, where each pixel is $\sim 0.5''$, and smoothed by a $40''$ Gaussian. A faint bridge of emission is connecting A98N and A98S. A98N appears to be slightly elongated in the N-S direction. The white box shows the region used to look for evidence of extended emission in Paterno-Mahler et al. (2014), and the white circles indicate r_{500} of the cluster they're centered on. Figure taken from Paterno-Mahler et al. (2014).

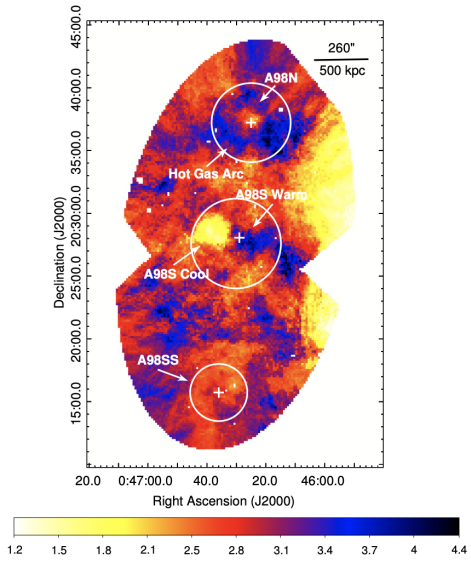

Figure 2.7: Temperature map of A98 with the scale bar in units of keV. The crosses mark the subcluster centers. A98N appears to have a cool core with a ring of warmer gas surrounding it. The enhancement is noticeable particularly to the south of A98N and north of A898S. This enhancement is possibly due to shock heated gas. A98S has an asymmetric temperature structure, with a local temperature minimum to the east and a local maximum to the west. Figure taken from Paterno-Mahler et al. (2014).

Paterno-Mahler et al. (2014) also searched for an intercluster filament in the region between A98N and A98S, however were unable to find evidence due to the low signal to noise of the relatively short observation.

CHAPTER 3

Methods

This chapter includes excerpts and figures from Alvarez et al. (2018) and Alvarez et al. (2022), used with permission from the Astrophysical Journal.

3.1 Data Reduction

This section will cover the data reduction routines employed in this work for *Chandra*,XMM-*Newton*, and *Suzaku*. Details of the *Chandra* observations explored for A3391/A3395 are presented in Table 3.1, and the observations explored for A98 are presented in Table 3.2.

Observatory	Pointing	ObsID	RA	Dec	Date Obs	Exposure [ks] ACIS-I EMOS1/EMOS2/EPN	PI
Chandra	A3391	4943	$06^h26^m22^s.20$	$-53^d41^m37^s.50$	2004-01-15	18.3	T. Reiprich
Chandra	Filament North	13525	$06^h25^m22^s.52$	$-53^d53^m54^s.09$	2012-08-18	48.4	S. Randall
Chandra	Filament Center	13519	$06^h26^m10^s.69$	$-54^d05^m08^s.53$	2012-08-17	47.1	S. Randall
Chandra	Filament South	13522	$06^h26^m46^s.24$	$-54^d17^m05^s.87$	2012-08-12	48.8	S. Randall
Chandra	A3395	4944	$06^h26^m49^s.56$	$-54^d32^m35^s.16$	2004-07-11	20.7	T. Reiprich
XMM-Newton	Filament Center	0400010201	$06^h26^m31^s.62$	$-54^d04^m44^s.7$	2007-04-06	38.2/38.5/23.1	M. Henriksen

Table 3.1: Summary of the *Chandra* and *XMM-Newton* X-ray pointings of A3391/A3395.

Observatory	Pointing	ObsID	RA	Dec	Date Obs	Exposure [ks] ACIS-I XIS0/XIS1/XIS3 MOS1/MOS2/PN	PI
Suzaku	A98C	809077010	$00^h46^m\ 29^s.93$	$+20^h33^m\ 25^s.9$	2014-06-09	59.75/58.86/59.63	S. Randall
Suzaku	A98N	809078010	$00^h46^m\ 18^s.12$	$+20^h50^m\ 20^s.0$	2014-07-02	-/-/24.9	S. Randall
Suzaku	A98N	809078020	$00^h46^m\ 18^s.02$	$+20^h50^m\ 21^s.1$	2014-07-03	23.3/21.1/22.5	S. Randall
Suzaku	A98N	809078030	$00^h46^m\ 19^s.18$	$+20^h49^m\ 43^s.3$	2014-12-21	48.9/50.3/51.5	S. Randall
Suzaku	A98S	809080010	$00^h46^m\ 42^s.48$	$+20^h16^m\ 30^s.0$	2014-12-20	47.7/48.4/49.0	S. Randall
Suzaku	A98W	809079010	$00^h45^m\ 15^s.40$	$+20^h40^m\ 10^s.2$	2014-07-03	95.6/96.9/99.7	S. Randall
Chandra	A98N	11877	$00^h46^m\ 24^s.80$	$+20^h28^m\ 05^s.0$	2009-09-17	19.5	S. Murray
Chandra	A98S	11876	$00^h46^m\ 29^s.30$	$+20^h37^m\ 17^s.0$	2009-09-17	19.8	S. Murray
Chandra	A98SS	12185	$00^h46^m\ 36^s.10$	$+20^h15^m\ 22^s.5$	2010-09-08	19.8	S. Murray
XMM-*Newton*	A98C	0652460201	$00^h46^m\ 13^s.40$	$+20^h34^m\ 47^s.5$	2010-12-26	33.0/33.0/24.0	C. Jones

Table 3.2: Details of the *Suzaku*, *Chandra*, and XMM-*Newton* observations of A98.

3.1.1 *Chandra Data Reduction*

The aimpoint for each *Chandra* observation investigated in this work was on the front-side illuminated ACIS-I CCD. CIAO version 4.8 and CALDB 4.7.2 are used for the A3391/A3395 observations, and CIAO version 4.9 and CALDB version 4.7.7 are used for the A98 observations, to reduce the data to level 2 event files with the *chandra_repro* script. The observations were taken in very faint (VF) mode and the background event files were filtered appropriately for VF mode. We use the CIAO tool *deflare* to remove periods of strong

flaring or data drop outs by removing periods where the light curve is more than 3σ from the mean. No instances of strong flaring in any of the observations are found. The total filtered ACIS-I exposure time for the A3391/A3395 observations is 183.3 ks, and 59.1 ks for the *Chandra* observations of A98 explored in this study.

3.1.2 XMM-*Newton* Data Reduction

Two different prescriptions for data reduction and analysis were used for this instrument, owing to the somewhat different goals of the analysis. The approach for each object are described separately.

3.1.2.1 A3391/A3395 Data Reduction

For the *XMM*-Newton data, photon events registered by the MOS1, MOS2, and PN detectors of European Photon Imaging Camera (EPIC) are gathered. In order to reduce the contamination of the source detections by soft protons, solar flare periods are excluded via a wavelet filtering of two event light curves extracted in the 10-12 and 1-5 keV energy band (Bourdin et al., 2005). The exposure times after filtering are shown in Table 3.1. Events registered by anomalously bright CCDs of the MOS cameras (Kuntz and Snowden, 2008) have also been removed for further analysis.

3.1.2.2 A98 Data Reduction

The Source Analysis Software (SAS) v18.0.0 is used to reduce the XMM-*Newton* event lists for the observations of A98N. The tools *odfingest* and *cifbuild* were used to create an ODF summary file, and to build a CIF file respectively in order to prepare the data for further analysis. The tool *xmmextractor* is then used to generate calibrated events files for point-like source analysis.

3.1.3 *Suzaku Data Reduction*

Suzaku observed the A98 system with 6 pointings (see Table 3.2) from June-December 2014. Three of the four XIS detectors, XIS0, XIS1, and XIS3, were on for each observation, as XIS2 was out of commission by this time.

The *Suzaku* data are reduced using HEASOFT version 6.22.1 and the latest calibration database as of May 2014. The FTOOL *aepipeline* is used for the first order reprocessing of the unfiltered files. Appropriate filters were applied for an Earth elevation greater than 5°, a sunlit Earth elevation greater than 20°, a cutoff rigidity greater than 6 GeV/c, and passages just before and after the South Atlantic Anomaly with *XSELECT*. The 5x5 editing mode files are first converted to the 3x3 editing mode using *xis5x5to3x3* and then the events are combined for each detector. The corners of the chips illuminated by the Fe^{55} calibration sources are then removed. The second rows from adjacent to the charge injected rows at 6 keV are removed from XIS1 for

further analysis due to the increase in NXB level on the back illuminated detector. Due to the micrometeorite hit to XIS0, the impacted region is excluded from the XIS0 field throughout the analysis. Light curves are extracted from the events files with the CIAO tool *dmextract*. The CIAO tool *deflare* is used on the light curves with the iterative sigma clipping routine *lc_sigma_clip* set to 3σ. No instances of strong flaring in these observations are found.

These *Suzaku* observations are found to be offset by $\sim 33''$ in right ascension from both the *Chandra* and XMM-*Newton* observations of the system. When analyzing data from the different observations jointly, this astrometry correction is taken into account.

3.2 Data Analysis

This section will discuss the data analysis performed on the end products described in Section 3.1

3.2.1 Imaging

3.2.1.1 *Chandra Imaging*

The *asphist, mkinstmap,* and *mkexpmap* routines in CIAO are used to generate aspect histograms, instrument maps, and exposure maps respectively for imaging. The blank sky background files with the closest observation periods to each of the *Chandra* observations are reprojected to match the observations using the CIAO routine *reproject_events*. The blank sky background images are hard-band (10-12 keV) scaled to match high-energy particle background count rate of the source observations. We use the *wavdetect* routine on wavelet scales of 2, 4, 6, 8, 10, 12, and 16 pixels, where the pixels are 0.98" in length to detect background point sources for removal. These sources are excluded from further analysis. The routine *dmfilth* is used to fill in the excluded source regions by drawing counts from a Poisson distribution matched to the local surrounding regions for imaging.

3.2.1.2 XMM-*Newton* Imaging

Two different imaging approaches were used for the two different studies. Both are described in the following two subsections.

3.2.1.2.1 A3391/A3395 XMM-*Newton* Imaging

3D event cubes are generated, wherein the events are sampled in position and energy. The resulting spatial binning is 1.6". Following the prescription presented in Bourdin and Mazzotta (2008), the event cubes contain information on the effective exposure and background noise values that are used for both imaging and spectroscopy.

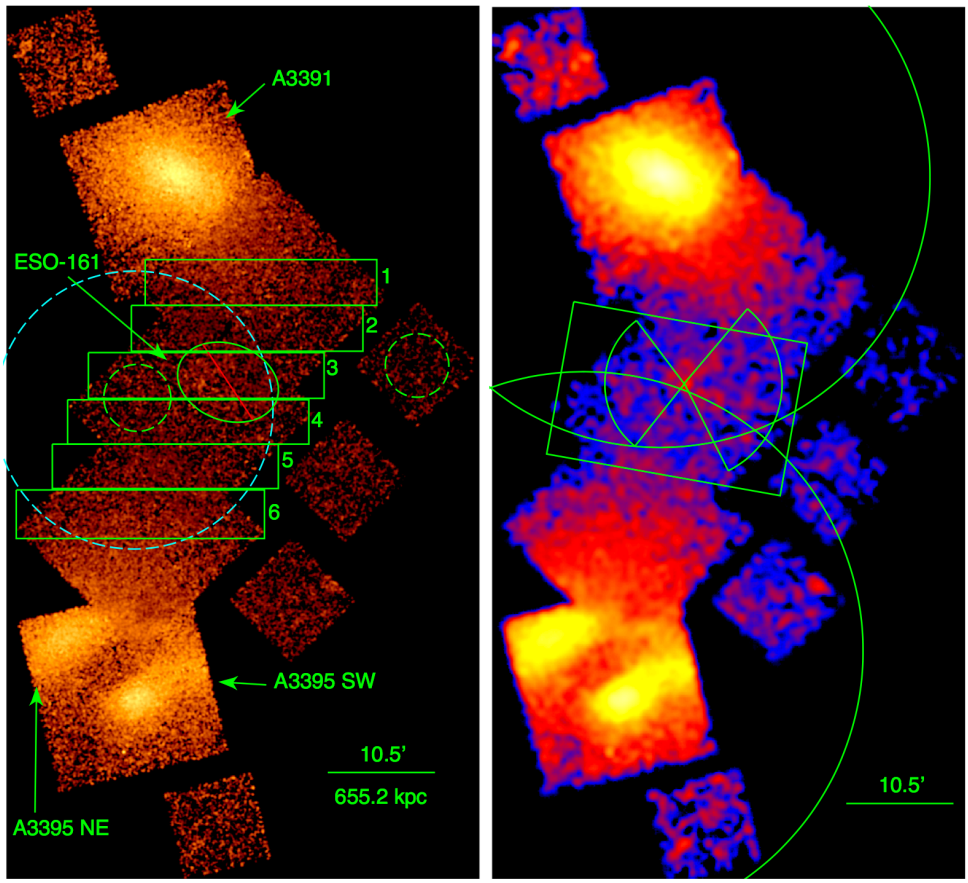

Figure 3.1: Left: The annotated background-subtracted exposure-corrected mosaic *Chandra* image of A3391/A3395, and the intercluster filament, is shown in the 0.3-7.0 keV energy band and smoothed by a $12''$ gaussian. The boxes denote regions used for the temperature profile of the filament. The excluded region, marked by the ellipse and red line, contains the galaxy group ESO-161. The green dashed circular region to the east of ESO-161 is used for local background modeling for the group temperature measurement. The green dashed circular region to the west is used for background in all *Chandra* spectral analyses. The XMM-*Newton* (see Table 3.1) field of view is shown in the dashed cyan region for reference. Right: Same as left but smoothed by a $40''$ gaussian to highlight the intercluster filament. Spectra extracted from the green box region were used to estimate the global temperature and density of the filament. The northern and southern circles are r_{200} for A3391 and A3395 respectively. The wedges are used to derive the surface brightness profile of the group.

The background noise model includes detections due to the detector fluorescence lines, cosmic induced particle background, and unresolved emission of astrophysical origin. This unresolved emission includes the cosmic x-ray background (CXB), and Galactic trans-absorption emission; see Kuntz and Snowden (2000). Spatial and spectral variations of the instrumental background are modeled for each detector following the prescription outlined in Bourdin et al. (2013). Amplitudes of the astrophysical emissions have been jointly fitted with the instrumental background in a sky region located to the northeast from the center of the *XMM-Newton* pointing, which is spatially separated from the A3391/A3395 system.

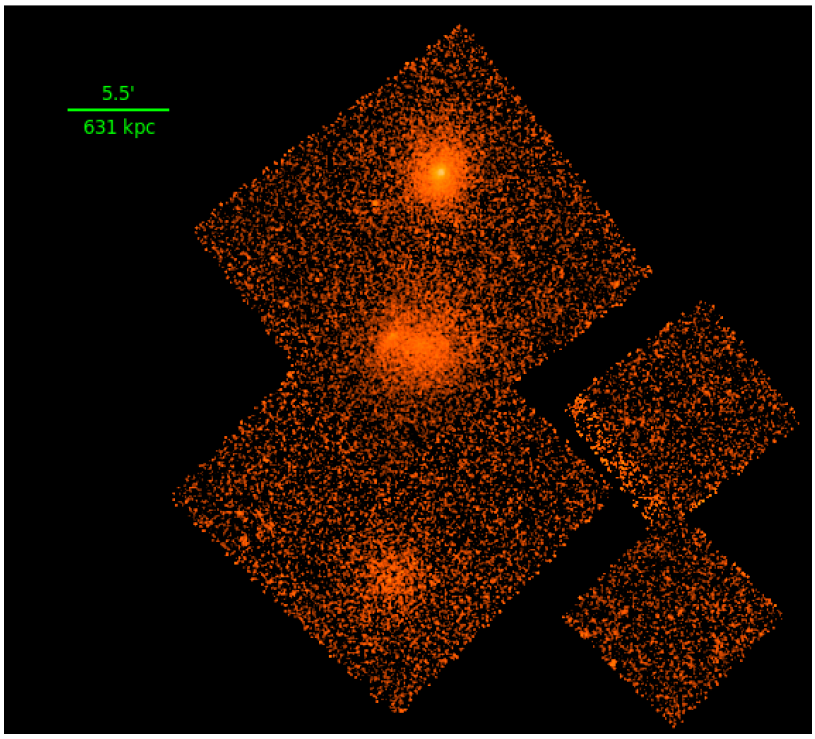

Figure 3.2: 0.3-7.0 keV blank sky background subtracted, exposure corrected, mosaic image of the *Chandra* observations of A98 (see Table 3.2). The image is smoothed with a $10''$ Gaussian.

Images and surface brightness profiles are corrected for the background noise model, as well as the effective exposure time expected within their energy band. For these purposes, effective exposures assume the incidental photon energy to follow the SED of an isothermal plasma of temperature kT=5 keV. To highlight the faint, diffuse emission, the exposure and background corrected photon image in Figure 3.3 has been smoothed by a gaussian kernel of width 19.2".

The image presented in Figure 4.1 of ESO-161 uses curvelet denoising to preserve and highlight surface brightness edges. Specifically, a curvelet transfrom of first generation (Candès and Donoho, 2002; Starck et al., 2003) is computed from the photon image (see the left panel of Figure 4.1). This transform combines ridgelet and wavelet bands, whose variance is stabilized following the Multiscale Variance Stabilized Transform proposed in Zhang et al. (2008). Variance stabilized coefficients of the exposure corrected photon image are subsequently thresholded at 3σ, which yields a boolean support of significant coefficients. To restore the source surface brightness, a curvelet transform of the background noise image is projected onto the significant coefficient support and subtracted from the thresholded transform of the photon image shown right panel of Figure 4.1.

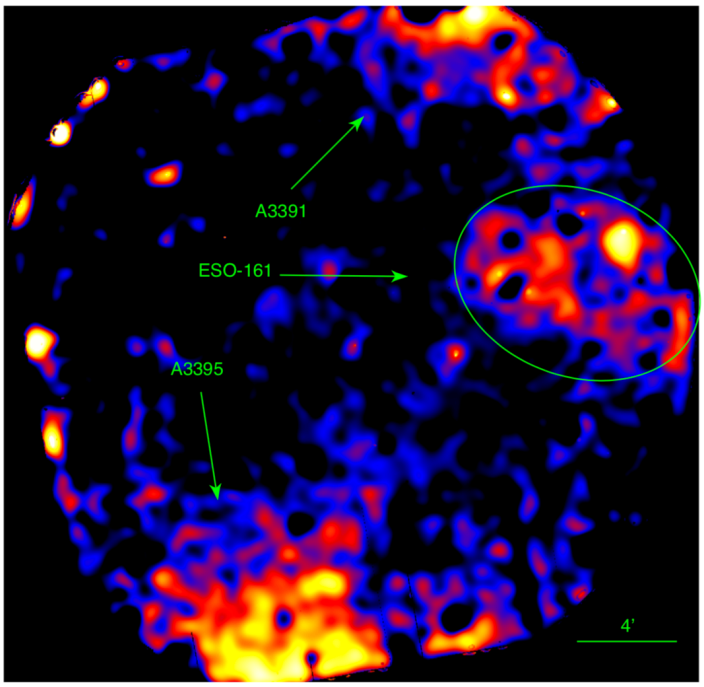

Figure 3.3: Log-scale *XMM-Newton* image of the A3391/A3395 intercluster filamentary region smoothed by a 19.6″ gaussian. This image is taken in the 0.3-2.5 keV band with MOS1, MOS2, and PN. The elliptical group region shown in Figure 3.1 (left panel) is shown for reference. Detected point sources are masked.

3.2.1.2.2 A98 XMM-*Newton* Imaging

A different approach was taken for this observation, as it was not used for modelling the diffuse emission in this system. The XMM-*Newton* observation of A98 was used only to model bright point sources. The tool *xmmextractor* is used to generate images for point-like source analysis. A smoothed 0.5-2.0 keV MOS2 image of this observation is presented in Figure 3.4.

3.2.1.3 *Suzaku Imaging*

The instrumental, non-X-ray background (NXB) images are generated using the *xisnxbgen* routine (Tawa et al., 2008). The NXB images are then scaled such that the hard-band (10-12 keV) count rate matches the

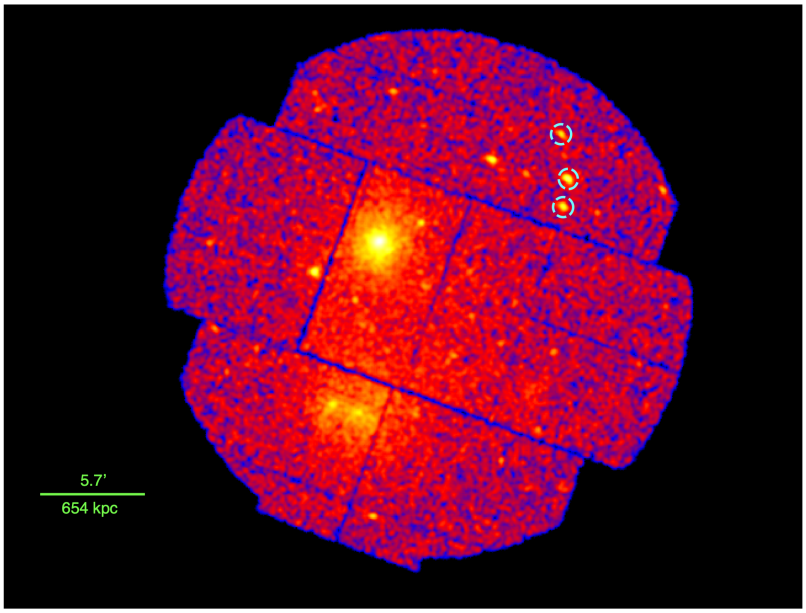

Figure 3.4: XMM-*N*ewton MOS2 image of A98N and A98S smoothed with a 15″ Gaussian kernel. The point sources modelled with XMM-*N*ewton data in this work are highlighted with dashed cyan regions.

source observations, as is done for the other instruments used in this work. After generating source and scaled NXB mosaic images, the mosaic NXB image is then subtracted from the source mosaic image. Flat field images are generated with the routine *xissim* to create effective exposure maps. The mosaic, NXB subtracted source image is divided by the mosaic exposure map to create the final image shown in Figure 3.5. The CIAO tool *wavdetect* is used on wavelet scales of 14 28 and 56 pixels, where each pixel is 2″ in length after binning. The image was then inspected by eye in order to make appropriate adjustments to the point source regions detected for exclusion from further analysis.

3.2.2 Spectroscopy

This section desctribes the spectroscopy methods that were performed with the end products (e.g. spectra, arfs, rmfs) described in Section 3.1

3.2.2.1 *Chandra Spectral Analysis*

The *specextract* tool with CIAO was used to extract spectra as well as the appropriate response files for analysis. All *Chandra* spectra in this work were grouped to a minimum of 40 net counts per bin.

XSPEC version 12.9.0 and XSPEC version 12.11.0 were used for A3391/A3395 and A98 respectively to perform the spectral analysis. Rather than use the CALDB blank sky files for background modeling, we use the circular westernmost region on the ACIS-I6 chip shown in the left panel of Figure 3.1 for A3391/A3395,

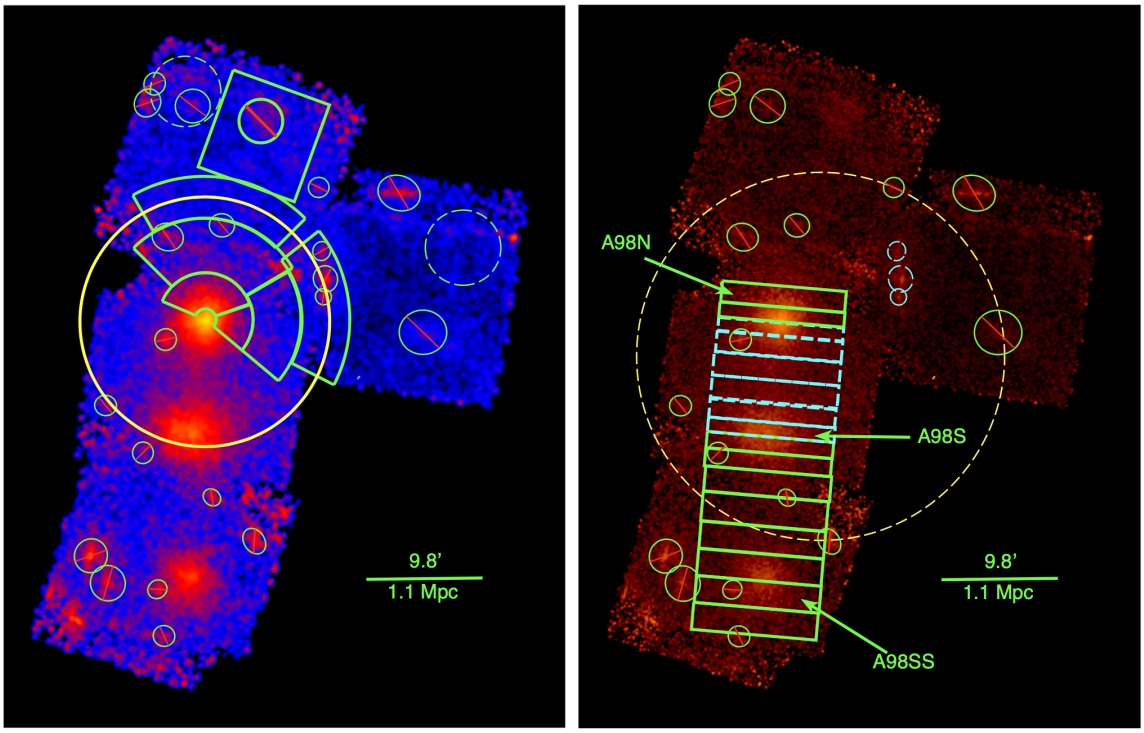

Figure 3.5: Left: Annotated, mosaic, background subtracted, and exposure corrected *Suzaku* image of the A98 system in the $0.5-7.0$ keV band. The image is binned to emphasize diffuse features in the system, and smoothed with a $20.8''$ guassian. The sectors are the regions used for the temperature and entropy profiles for A98N. The yellow circle denotes r_{200} for A98N derived from the T_{500}-r_{500} relation found by Vikhlinin et al. (2009). The dashed green circles are regions used to constrain the sky background. The excluded regions are point sources, with the exception of a potential background cluster (see Chapter 4), and are excluded from further analysis. The cyan dashed circle regions mark the point sources that are modelled simultaneously with the outermost sector to the west of A98N. The box region to the north is used to estimate large-scale properties described in Chapter 4. Right: The *Suzaku* image is smoothed with a $10.4''$ circular guassian. The box regions are used for the intercluster filament thermodynamic profiles presented in Chapter 4. The dashed cyan boxes are used to derive the temperature, electron density, and entropy profile for A98N and A98S presented in Figure 5.4. The dashed yellow circle denotes the XMM-*Newton* field of view. The cyan dashed regions and exclusion regions are the same as in the left panel.

and a circular region on the southernmost ACIS-I6 chip for A98. This has advantages over the blank sky background files, which are a sky average rather than the background in a nearby region of the sky.

The stowed *Chandra* background files, in which long exposures were taken with ACIS stowed and in VF mode, are used for instrumental background in the spectral fitting with an applied hard-band (10-12 keV) correction as was done for the blank sky background files for imaging. The scaled stowed spectra are consequently subtracted from the source spectra and local sky background spectrum during spectral modeling. The stowed dataset accurately represents the quiescent, non-X-ray background (NXB), and this dataset introduces an additional $\pm 2\%$ statistical uncertainty (for more information on the stowed dataset we refer the reader to Hickox and Markevitch (2006)). For our faintest region in the A3391/A3395 observations, the effect that the

systematic NXB uncertainty has on our measured kT and XSPEC normalization error range is an increase of less than 10% and less than 3% respectively. This effect is much smaller than the statistical errors in this region, so we do not include the systematic NXB uncertainty in our error budget.

The local sky background spectrum (see left panel of Figure 3.1) is simultaneously fit with the source spectra to include background uncertainties in the calculated error ranges. An absorbed Astrophysical Plasma Emission Code (APEC) (Smith et al., 2001) model was used for the source spectra. The background spectra were simultaneously fit, along with the source spectra, with an absorbed powerlaw (PL) for the cosmic X-ray background, an absorbed APEC model for the galactic halo (GH), and an unabsorbed APEC model for the local hot bubble (LHB). The ICM, GH, and CXB are absorbed assuming a Galactic Hydrogen density column of $N_H = 6.3 \times 10^{20}$ cm^{-2} for A3391/A3395 and $N_H = 3.0 \times 10^{20}$ cm^{-2} for A98 found with the ftool *nh* (Kalberla et al., 2005). See Section 3.2.2.4 for more details.

3.2.2.2 *Suzaku Spectral Analysis*

To extract spectra for the *Suzaku* observations, the data is loaded into the *XSELECT* environment and subsequently the *extract spec* routine is utilized. Then the corresponding redistribution matrix file (RMF) is generated with *xisrmfgen*. The RMF and source spectrum are then used to generate the ancillary response files (ARFs) with *xissimarfgen*.

Two different ARFs are generated for each spectrum to be folded into two different model components in the spectral fits; the source model and the background model. The *Chandra* image is used to fit a 2D beta model for all three clusters. In order to create more accurate ARFs for the source spectra, *xissimarfgen* utilizes an image of the 2D beta model. A uniform circle with a radius of $20'$ is used to generate the ARFs folded into the background model, under the assumption that it is uniform.

Non X-ray background (NXB) spectra are generated with *xisnxbgen* (for more details see (Tawa et al., 2008)) and are subtracted from the source spectra in *XSPEC*. We group all of our spectra such that each bin contains a minimum of 40 counts. The free model parameters can be seen in Table 3.3. The LHB temperature is fixed to $kT = 0.1$ keV, and the powerlaw component for the CXB is fixed to $\Gamma = 1.4$.

BG Region	CXB Norm [photons/keV/cm^2/s/arcmin^2]	GH kT [keV]	GH Norm [cm^{-5}arcmin^{-2}]	LHB Norm [cm^{-5}arcmin^{-2}]
West	$6.9e-7^{+4e-8}_{-4e-8}$	$0.19^{+0.03}_{-0.01}$	$1.3e-6^{+8e-7}_{-3e-7}$	$2.1e-7^{+1e-7}_{-2e-7}$
North	$6.8e-7^{+3e-8}_{-3e-8}$	$0.19^{+0.04}_{-0.02}$	$1.4e-6^{+8e-7}_{-4e-7}$	$1.8e-7^{+1e-7}_{-1e-7}$

Table 3.3: The free parameters for the fits to the dashed green background regions shown in Figure 3.5 (Left).

Most point sources are removed by inspecting the *Suzaku*, *Chandra*, and XMM-*Newton* observations listed in Table 3.2. The bright point sources that are not excluded from the regions for analysis are modelled simultaneously. We first model the point sources shown in Figure 3.5 Right with an absorbed powerlaw model

for AGN, and an APEC model for a foreground galactic star, using the XMM-*Newton* data that overlaps the *Suzaku* field of view (FOV). We then take the parameters from the model to simulate the same *Suzaku* point source with the FTOOL *xissim*. We use this simulation to estimate the *Suzaku* normalization for the point source models and then fold the point source models into the region fits, allowing the point source parameters to vary within their 90% errors derived from the XMM-*Newton* fit of the source.

3.2.2.2.1 *Suzaku* Scattered Light

Due to *Suzaku's* relatively large PSF, one must consider the effects of scattered light from adjacent regions when performing spectral analysis. In order to determine the effect of scattered light across adjacent regions, we use *xissim* to simulate each region with 2×10^6 photons as is done in e.g. Walker et al. (2012) and Bulbul et al. (2016). We calculate the percentage of photons that originate from the region of interest and are detected in that region, and what percentage of photons are scattered into the adjacent region in order to include a properly weighted component in the spectral fit to the adjacent region (Table 3.4). We use these values to test whether the scattered light affects our results, particularly in the faintest regions analyzed in this work. We find that the scattered light does not change the final results for the analysis of A98N, as the statistical error dominates the effect of scattered light. We find that the scattered light from outside of the FOV is negligible. Therefore, we omitted values from Table 3.4 where the adjacent sector was outside of the FOV of the observation containing the source sector.

Region	N01	N02	N03	W01	W02	W03
N01	65.1	-	-	-	-	-
N02	-	73.2	6.69	-	-	-
N03	-	9.38	70.6	-	-	-
W01	-	-	-	54.5	6.2	-
W02	-	-	-	9.86	60.0	-
W03	-	-	-	-	-	60.7

Table 3.4: Percentage of light scattered from the regions in the columns into the regions in the rows. "N" represents the sectors to the north of A98N, and "W" represents the sectors to the west of A98N.

3.2.2.3 XMM-*Newton Spectral Analysis*

3.2.2.3.1 A3391/A3395 XMM-*Newton* Spectral Analysis

Amplitudes of the astrophysical emissions have been jointly fitted with the instrumental background in a sky region located to the northeast of the *XMM-Newton* pointing, which is spatially separated from the A3395-A3391 intercluster filament.

Spectroscopic measurements similarly rely on modeling the source emission measure provided by the APEC model. We similarly assume elemental abundances follow the solar composition tabulated in Grevesse and Sauval (1998) and the Spectral Energy Distribution (SED) of the intercluster plasma is redshifted to

z=0.0530. The ICM, GH, and CXB are absorbed assuming the Galactic Hydrogen column density reported in Section 3.2.2.1. The LHB is unabsorbed. For the CXB, the power-law index was fixed at 1.4, while the temperatures of the LHB and GH were fixed at 0.1 keV and 0.3 keV respectively. The normalizations are free to vary. The background model was fit simultaneously with the source model and the normalizations are generally consistent with the *Chandra* background normalizations within 2σ (see Table 3.5). In this modeling, all astrophysical components are corrected for spatial variations of the instrument effective area and redistributed as a function of the energy response of the detectors.

[b]

Component	kT/Γ [keV]/Γ	N [cm^{-5}/photons keV^{-1} cm^{-2} s^{-1} at 1 keV] (*Chandra/RASS*)
LHB	$0.092^{+0.06}_{-0.05}$	$1.55^{+8.0}_{-0.17} \times 10^{-5}$
GH	$0.37^{+0.31}_{-0.09}$	$2.2^{+0.76}_{-0.92} \times 10^{-5}$
PL	1.4^{f}	$2.7^{+0.55}_{-0.58} \times 10^{-5}/2.1^{+0.28}_{-0.35} \times 10^{-3}$

f fixed parameter
Γ photon index

Table 3.5: CXB and foreground components derived from a spectral fit of RASS data as well as Chandra data from the green dashed region on the ACIS-I6 chip (see the left panel of Figure 3.1) without contamination from source data.

3.2.2.3.2 A98 XMM-*Newton* Spectral Analysis

SAS is used to generate all of the necessary files of the point-like (background active galactic nuclei (AGN), and stars) regions shown in Figure 3.4 for analysis in *XSPEC*. In order to generate the source and background spectra, we use the *evselect* routine. We then use the *rmfgen* routine to generate the redistribution matrix files and the *arfgen* routine to generate the ancillary response file for the spectrum. The XMM-*Newton* spectra are grouped such that each bin contains a minimum of 25 counts due to the relatively low counts observed for the point sources. We then use an absorbed powerlaw model in *XSPEC* for the point sources that are AGN, and a simple APEC model a point source that is galactic foreground star.

3.2.2.4 Background and Foreground

This subsection will describe the background and foreground parameters that must be taken into account, especially for such low surface brightness emission. This includes the galactic halo, local hot bubble, and cosmic x-ray background.

3.2.2.4.1 Systematic Error in the Cosmic X-ray Background

For the faint, diffuse emission that is characterized in this work, accurate modeling of the cosmic X-ray background (CXB) is essential. X-ray telescopes resolve point sources only as well as the distribution of the

point spread function (PSF) allows. *Chandra* particularly resolves point sources well (on-axis PSF $\sim 0.5''$), but still only to a limiting flux, which is different for on versus off axis observations. The PSF for *Suzaku* is broader, with an on-axis value of $\sim 2'$. The fainter, unresolved point sources contribute flux that needs to be characterized. For the on-axis observations, we adopt the methodology for estimating the total flux from the unresolved CXB that Bautz et al. (2009), Bulbul et al. (2016) and Walker et al. (2012) implement in similar analyses using *Suzaku* data, which we describe here.

The *Chandra* filament observations of A3391/A3395 allow us to detect point sources down to a flux of $S_{lim} = 1.4^{+2.6}_{-0.6} \times 10^{-15}$ ergs cm^{-2} s^{-1}. For comparison $S_{lim} \approx 10^{-13}$ ergs cm^{-2} s^{-1} is a typical value for moderately deep *Suzaku* (e.g. Walker et al., 2012). Moretti et al. (2003) defines the unresolved CXB flux in ergs cm^{-2} s^{-1} deg^{-2} as:

$$F_{CXB} = (2.18 \pm 0.13) \times 10^{-11} - \int_{S_{lim}}^{S_{max}} \frac{dN}{dS} \times S \, dS. \tag{3.1}$$

The analytic form of the total unresolved source flux distribution in the 2-10 keV band is characterized as:

$$N(>S) = N_0 \frac{(2 \times 10^{-15})^{\alpha}}{S^{\alpha} + S_0^{\alpha-\beta} S^{\beta}} \text{ deg}^{-2}, \tag{3.2}$$

where $\alpha = 1.57^{+0.10}_{-0.18}$ and $\beta = 0.44^{+0.12}_{-0.13}$ are the power law indices for the bright and faint components of the distribution respectively, $N_0 = 5300^{+2850}_{-1400}$, S_{lim} is the flux of the faintest point source detected in the observations, and S_{max} is 8×10^{-12} ergs cm^{-2} s^{-1}. We find the unresolved CXB in the A3391/A3395 *Chandra* observations has an expected total flux of $7.5 \pm 2.1 \times 10^{-12}$ ergs cm^{-2} s^{-1} deg^{-2}. The unresolved CXB in the background region used in the *Suzaku* observations has a flux of $1.87 \pm 0.13 \times 10^{-11}$ ergs cm^{-2} s^{-1} deg^{-2}.

An additional systematic uncertainty is spatial variance due to for example the distribution not being uniform on small scales, or individual sources just below the detection limit falling into a region used for analysis. The expected 1σ spatial uncertainty in the total unresolved CXB flux is given by:

$$\sigma^2 = \frac{1}{\Omega} \int_0^{S_{lim}} \frac{dN}{dS} \times S^2 \, dS \tag{3.3}$$

where Ω is the solid angle (Bautz et al., 2009). This method is used to constrain the normalization of the CXB component of the background, and allow this parameter to vary within the derived 1σ errors.

3.2.2.4.2 *Rosat* All Sky Survey Annuli

A *Rosat* All Sky Survey (*RASS*)[1] spectrum was also extracted from an annulus with an inner radius of 1° and an outer radius of 1.1° centered around ESO-161 from the *RASS* observation of A3391/A3395 in order to better constrain the local sky background parameters in our spectral fits. We extract a *RASS* spectrum of an annulus centered on RA = $0^h46^m18^s.8872$ and Dec = $20^h28^m13^s.557$, approximately on the X-ray centroid of A98SS, with an inner radius of 0.5643° and an outer radius of 0.6738° for A98. These spectra were simultaneously fit as part of the background model throughout the x-ray analyses.

[1] https://heasarc.gsfc.nasa.gov/cgi-bin/Tools/xraybg/xraybg.pl

CHAPTER 4

Results

This chapter includes excerpts and figures from Alvarez et al. (2018) and Alvarez et al. (2022), used with permission from the Astrophysical Journal.

4.1 A3391/A3395

Here the results found for A3391/A3395 are presented. See Chapter 5 for further discussion on these findings.

4.1.1 A3391/A3395 Bridge Thermodynamic Properties

As stated in Chapter 2, A3391 is the cluster located to the north, while A3395 is located to the south. There is an extended filament of hot X-ray gas connecting the main clusters (see e.g. Figure 3.3). ESO-161 is a galaxy cluster located in between the two clusters, and is most clearly seen in Figures 4.1 and 4.2, along with the extended diffuse emission in Figure 3.3 indicated inside the group ellipse region.

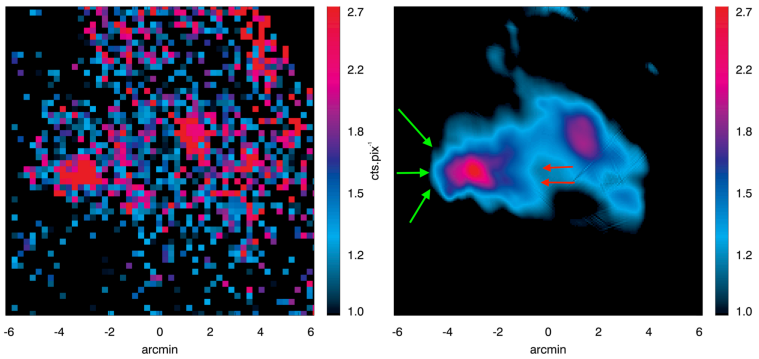

Figure 4.1: *XMM-Newton* images of ESO-161 in the 0.3-2.5 keV energy range. The color bar is counts/pixel. Left: The original *XMM-Newton* photon image of ESO-161 with 14.4″ pixels. Right: Curvelet denoised at the 3σ level *XMM-Newton* image of ESO-161 derived from the left photon image. The green arrows indicate the eastern leading edge. The red arrows indicate the downstream edge discussed in Chapter 5.

The megaparsec-scale bridge connecting the main subclusters is highlighted in Figure 3.1 (right panel) and Figure 3.3 (for a wider field of view, see e.g. Section 3.2.1.2.1). The box regions shown in Figure 3.1 (left panel) are used for the temperature, abundance, density, and entropy profiles presented in this Section.

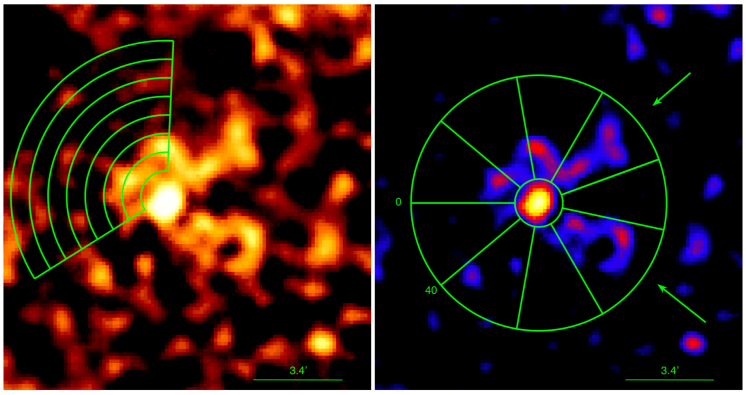

Figure 4.2: Close up *Chandra* image of ESO-161 of Figure 3.1 (right panel). Left: ESO-161 with the annuli used for a surface brightness profile (see Chapter 5) overlaid. Right: The overlaid azimuthal region is used for a surface brightness profile (see Chapter 5). The arrows indicate where the two possible stripped gas tails are located.

To measure a gas mass, electron density, and temperature for the whole filament, the box region shown in Figure 3.1 (right panel) is used to extract the spectra in Figure 4.3. The black, red, and green lines are the source spectra corresponding to ObsIDs 13525, 13519, and 13522 respectively. The dark blue line is the sky background spectrum, which was simultaneously fitted, for the green dashed region on the ACIS-I6 chip for ObsID 13525 in the left panel of Figure 3.1. The light blue line is the *RASS* annulus background spectrum, which was also simultaneously fitted. The soft excess in the residuals for the local *Chandra* background component is recognized; however adding a soft proton component to the model does not improve the fit. Letting the GH and LHB parameters vary untied between spectra removes this soft excess for the I6 background spectrum in the residuals, however then the GH and LHB model parameters are then in tension with each other. Due to the low S/N of the I6 spectrum ($\sim 15\%$), we choose to leave these parameters tied. Performing either of these analyses, however, does not significantly change the best fit parameter values or error ranges.

For all reported gas masses in this system, a 3D cylindrical geometry for the filament is assumed, with the length and radius dimensions corresponding to the box region length and half-width edges respectively, assuming that the filament is slightly more extended than what is encompassed within the $16'$ by $16'$ *Chandra* field of view and fills the box region. The box region in Figure 3.1 (right panel), for a 3D cylindrical geometry has a radius of 0.7 Mpc and a length of 0.9 $\sin(i)^{-1}$ Mpc, where i is the inclination angle of the filament to

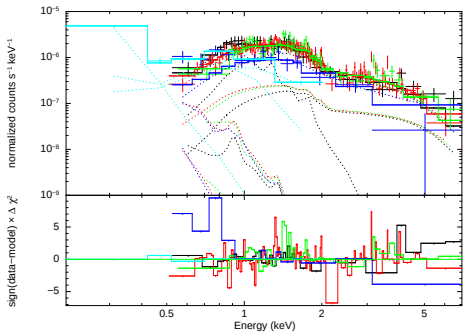

Figure 4.3: Top: The best fit spectrum for the box shown in the right panel of Figure 3.1. The black, red, and green lines are from ObsIDs 13525, 13519, and 13522 respectively. The dark blue line is the simultaneously-fitted background spectrum for the dashed region on ObsID 13525 shown on the ACIS-I6 chip in the left panel of Figure 3.1. The light blue line is the simultaneously-fitted background *RASS* spectrum. Bottom: Residuals for the top spectra. Dotted lines are model components.

the line of sight. The box region was placed where the filament emission is relatively bright and where the ICM emission is relatively faint, thus maximizing the S/N of the filament emission. The box regions used for the profiles in Figure 3.1 (left panel) were assumed to have a 3D cylindrical geometry with radii of 0.7 Mpc and a length of 0.3 $\sin(i)^{-1}$ Mpc. The electron density of the filament is derived from the normalization in XSPEC, and is given by:

$$n_e = \left[1.2\,N \times 4.07 \times 10^{-10}(1+z)^2 \left(\frac{D_A}{\mathrm{Mpc}}\right)^2 \left(\frac{V}{\mathrm{Mpc}^3}\right)^{-1}\right]^{1/2}, \tag{4.1}$$

where D_A is the angular distance to the system, r is the radius of the filament, l_{obs} is the observed projected length of the filament, and N is the XSPEC normalization. The electron density profile across the filament is shown in Figure 4.4.

The aforementioned box region (see right panel of Figure 3.1) was best fit with a two temperature APEC model ($\chi^2/dof = 619.46/594$) rather than a one temperature APEC model ($\chi^2/dof = 714.96/595$). The projected temperatures for the best two temperature fit are found to be kT = $4.45^{+0.89}_{-0.55}$ keV and $0.29^{+0.08}_{-0.03}$ keV. Under the assumption that the hotter temperature component is that associated with the filament (see Chapter 5 for discussion), we find an electron density $n_e = 1.08^{+0.06}_{-0.05} \times 10^{-4}\ \sin(i)^{\frac{1}{2}}$ cm^{-3}, and $M_{\rm gas} = 2.7^{+0.2}_{-0.1} \times 10^{13}\ \sin(i)^{-\frac{1}{2}}$ M$_\odot$ for the filament assuming that this inferred density extends outside the *Chandra* FOV into the box region shown in Figure 3.1. If the filament is indeed completely covered by the *Chandra* FOV and is not extended, then the gas mass would be $\sim 1.7 \times 10^{13}\ \sin(i)^{-\frac{1}{2}}$ M$_\odot$. This gas mass is in good agreement with Tittley and Henriksen (2001). Note that the reported errors are statistical; there are additional systematic

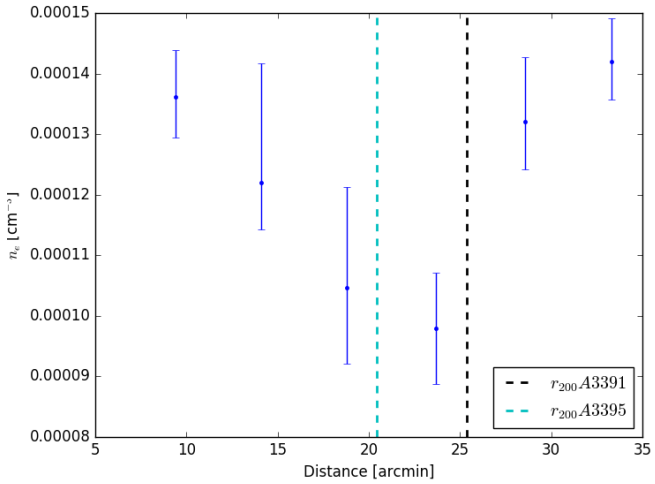

Figure 4.4: The electron density profile for the filamentary region derived from the 1T model normalizations. The black and cyan dashed lines are r_{200} for A3391 and A3395 respectively. The X-axis is the distance from the center of A3391.

errors associated with the assumed cylindrical geometry and unknown substructure of the filament.

The mean baryonic density of the universe at $\bar{z} = 0.053$ is $\bar{\rho}_{baryon} \simeq 4 \times 10^{-31}$ g cm^{-3}. If the filament is in the plane of the sky (see Chapter 5), $\frac{\rho_{fil}}{\bar{\rho}_{baryon}} \lesssim 541$. If the filament is indeed aligned close to the plane of the sky, this overdensity is not consistent with that expected for the WHIM gas, which is thought to range between 1-250 (Bregman, 2007).

The boxes shown in Figure 3.1 (left panel) are used to extract spectra and create the projected one temperature (1T) profile. In Figure 4.5, three temperature profiles are displayed; two *Chandra* profiles including the group and excluding the group ESO-161, and the XMM-*Newton* profile also excluding the group region.

Additionally, a two temperature (2T) APEC model is fit for the same spectra in each of the regions in the profile, keeping the metallicity fixed at $0.2Z_{\odot}$. Fitting a second cool component to the spectrum of the northern filament observation only for regions 2 and 3 yields better statistically significant 2T fits shown in

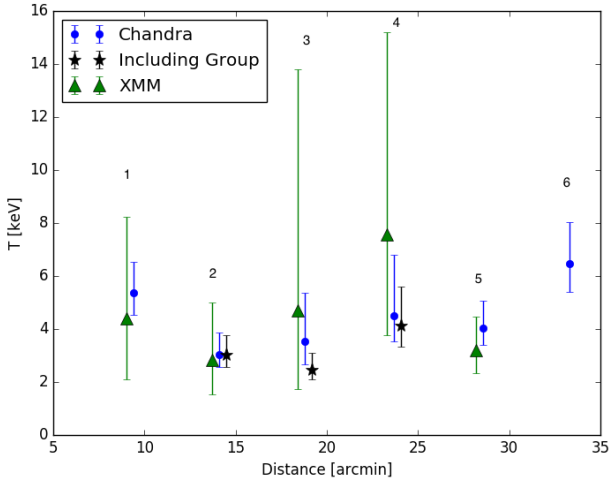

Figure 4.5: The projected temperature from *Chandra* and *XMM-Newton* observations as a function of distance from the center of the northern subcluster, A3391. Each point corresponds to a box region from which we extracted spectra (see the left panel of Figure 3.1). The black points include the group emission and offset for viewing purposes. The green triangles are the *XMM* measurements and the blue circles are the *Chandra* measurements. Regions are labeled for reference.

Table 4.1 (see Chapter 5 for discussion).

Reg	kT_1 [keV]	N_1 (10^{-4}) [cm^{-5}]	kT_2 [keV]	N_2 (10^{-4}) [cm^{-5}]	χ^2/dof
2	$3.03^{+0.88}_{-0.49}$	$9.38^{+0.10}_{-0.50}$	...	...	359.51/328
2	$4.77^{+2.24}_{-1.21}$	$7.27^{+0.68}_{-0.71}$	$0.44^{+0.17}_{-0.10}$	$6.74^{+3.23}_{-2.58}$	301.83/327
3	$3.53^{+1.85}_{-0.87}$	$7.10^{+0.84}_{-0.64}$	...	...	203.55/211
3	$3.87^{+2.46}_{-1.00}$	$7.15^{+1.24}_{-0.69}$	$0.28^{+0.15}_{-0.09}$	$3.89^{+8.49}_{-2.47}$	183.87/210

Table 4.1: The best fit parameters for 1 and 2 temperature models for regions 2 and 3 in the 0.5-7.0 keV band.

A best fit 1T model is found, with projected temperature $kT = 4.49^{+2.31}_{-0.97}$ keV, and electron density $n_e = 9.79^{+0.92}_{-0.92} \times 10^{-5} \sin(i)^{\frac{1}{2}}$ cm^{-3} for Region 4. This is the only area in this study that lies approximately at r_{200} of both of the subclusters. Figure 4.6 shows the spectrum for Region 4, where the black (13519) and

red (13522) lines are the source spectra, the green line (13525) is the simultaneously fit dashed background region (see the left panel of Figure 3.1), and the blue line is the simultaneously fit background *RASS* spectrum.

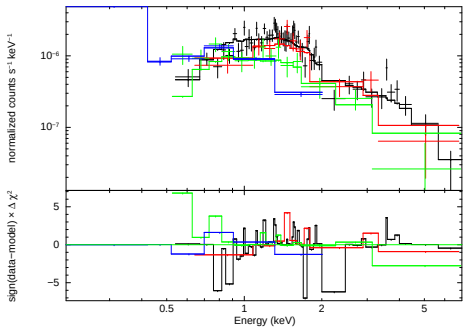

Figure 4.6: Spectral fit and the residuals for Region 4, located approximately at r_{200} for both clusters, shown in the left panel of Figure 3.1. The black and red lines are the source spectra from north to south respectively, the green line is the simultaneously fitted dashed background region (see the left panel of Figure 3.1), and the blue line is the simultaneously fitted background *RASS* spectrum. Figure and caption are taken from Alvarez et al. (2018) with permission.

Upper limits of the projected abundances for regions 1, 3, 4, and 6 shown in the left panel of Figure 3.1 derived from an absorbed APEC model are displayed in Table 4.2.

Region	Abundance $[Z_{\odot}]$
1	< 0.72
2	$0.14^{+0.12}_{-0.12}$
3	< 0.63
4	< 0.65
5	$0.60^{+0.74}_{-0.20}$
6	< 0.63

Table 4.2: Projected abundance values for the box regions shown in Figure 3.1 (left panel).

The temperature profile along the intercluster filament derived from XMM-*Newton* observations is in good agreement within uncertainties with the Chandra results. Region 6 is not fit with the XMM-*Newton* data, as the region is only covered by EMOS1 after the filtering of bright CCDs, and the signal to noise is too low to constrain the fit. The large uncertainties for Region 3, and to a lesser extent Region 4, are a result of excluding the group region and subsequently having low areal coverage of the observation (see the left panel of Figure 3.1), as well as a low inherent S/N as Region 4 is the faintest region. The temperature, abundance, and density profiles (see Chapter 5) are also in good agreement with those found with *Suzaku* in Sugawara et al. (2017).

4.1.2 ESO-161

The galaxy group ESO-161 found in the intercluster filament has extended emission mostly to the west, which can be seen in Figures 3.3, and 4.2.

The surface brightness profile in the east-west direction across ESO-161 can be seen in Figure 4.7, derived from the region marked by wedges in Figure 3.1 (right panel). Here, the annuli are equally spaced bins of $0.6'$. Note that the x-axis origin, $0'$, of the surface brightness profile corresponds to the center of the annuli, with the west wedge noted as positive arcminutes and the east wedge is negative arcminutes. The goal of this analysis was to discern where the group emission reached the background emission. Therefore, a cut was made where the surface brightness profile flattens out at $\approx 8'$ to the west and at $\approx 3'$ to the east. The XMM-*Newton* image was then examined to refine the group region by eye as it is shown in Figure 3.1 (left panel). The group emission is elliptical and slightly angled in the NE-SW direction.

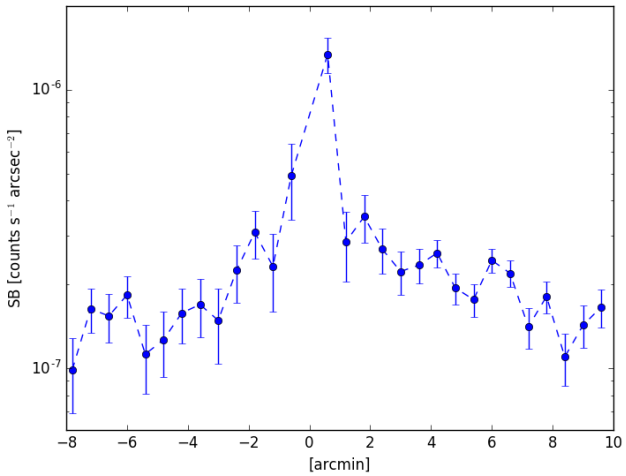

Figure 4.7: Surface brightness profile in the 0.3-2.5 keV band of ESO-161 extracted from the *Chandra* observations with the wedges shown in the right panel of Figure 3.1. Errors are 1σ.

4.2 A98

4.2.1 A98N in Partial Azimuth

In this section we present temperature, electron density, and entropy profiles for regions shown in Figure 3.5.

The electron density of regions of interest is similarly derived from the normalization for the APEC model in *XSPEC*, as is described in Section 4.1.1.

4.2.2 Cluster Thermodynamic Properties

Here the thermodynamic profiles of the subclusters in the A98 system are presented. In order to deproject the temperature measurements, the "onion peeling" method (Ettori et al., 2010) is used. A spherical geometry for the galaxy cluster components in the system is assumed.

The *Suzaku* temperature profile of A98N in partial aziumth (see sector regions in e.g. Figure 3.5 (Left)) is shown in Figure 4.8 as well as the "Universal" temperature profile (Ghirardini et al., 2019) expected based upon the average electron temperature of the system. While not all of the error constraints are tight, the temperature profile of A98N is not only consistent in partial azimuth, but also seems to adhere to expectations of the temperature profile based on average cluster temperature (cluster T_{500} measurements with *Suzaku* are presented in Table 3.2).

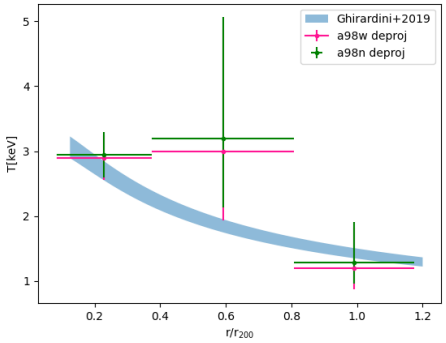

Figure 4.8: The deprojected temperature profile of A98N for the sectors to the north and west shown in Figure 3.5. The pink points are for the sectors to the west of A98N and the green points are for the sectors to the north of A98N. The blue line is the "Universal" temperature profile presented in Ghirardini et al. (2019).

The electron density profile of A98N in the northern and western sectors is shown in Figure 4.9. The profiles are consistent with each other within errors.

The deprojected entropy profiles for A98N in the northern and western sectors, for the regions shown in e.g. Figure 3.5 (Left), are shown in Figure 4.10. Here, entropy is defined as $K = kT_e n_e^{-2/3}$, where k is Boltzmann's constant, T_e is the measured electron temperature, and n_e is the derived electron density assuming a region appropriate volume as described in Equation 4.1.

We find that, in both sectors, the entropy values for A98N are consistent with the self-similar prediction of pure gravitational collapse, based upon spherical hydrodynamic (SPH) simulations of galaxy clusters, near the virial radius, in which entropy $K \propto r^{1.1}$ (Voit et al., 2005). There is some hint of entropy flattening,

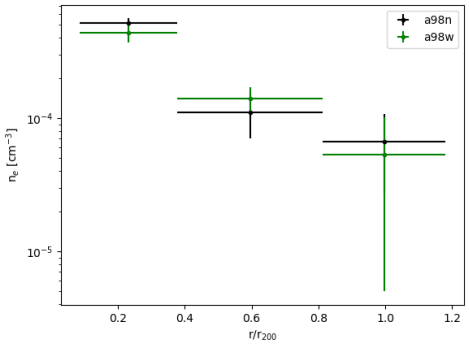

Figure 4.9: The electron density profile of the annuli to the north and west of A98N (see e.g. Figure 3.5 (Left)).

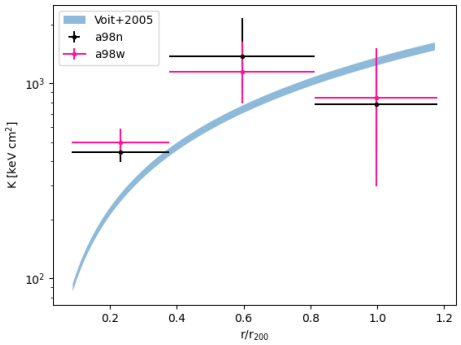

Figure 4.10: The blue line is the entropy profile expected from pure gravitational collapse (Voit et al., 2005) for A98N. The black points are for the sector regions to the north of A98N and the pink points are for the sector regions to the west of A98N shown in Figure 3.5.

however the errors on the entropy are too large to say definitively. This is in agreement with similar studies of lower mass systems (e.g. Su et al., 2015; Bulbul et al., 2016; Sarkar et al., 2021) even though A98N is most likely undergoing a merging event (Paterno-Mahler et al., 2014; Sarkar et al., 2022). At small cluster radii ($r < r_{500}$), the entropy for A98N is above that expected for self-similarity. This excess is consistent with what is seen in other systems, particularly lower mass systems (Sun et al., 2009), and is likely due to the effect of non-gravitational processes in the central region (e.g. AGN feedback (e.g. O'Sullivan et al., 2011)).

4.2.2.1 A98N-A98S Bridge

To investigate whether the apparent surface brightness enhancement in between A98N and A98S is due to two cluster halos overlapping, we compare the combined surface brightness profiles of A98N and A98S to the emission across the bridge, as done in (Paterno-Mahler et al., 2014; Sarkar et al., 2022) .

The background subtracted surface brightness profiles of the box annuli to the north of A98N and to the

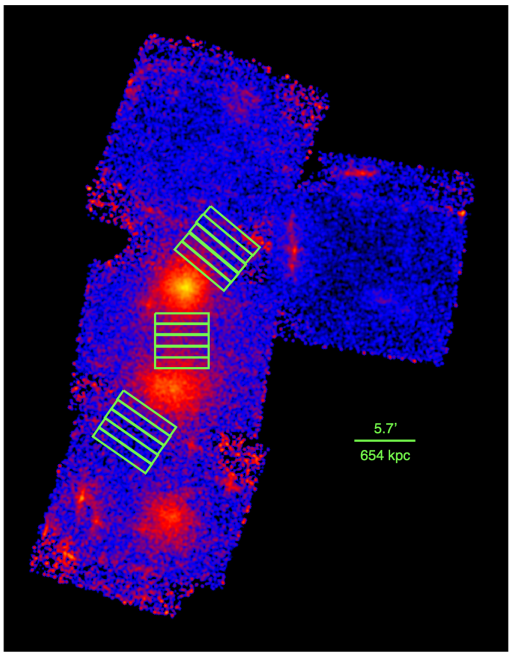

Figure 4.11: Same as Figure 3.5: Left, but instead smoothed with a 12.5″ Gaussian. The rectangular annuli to the north of A98N and to the south of A98S are used to compare the combined surface brightness of the two clusters to the box regions in the bridge region (see Figure 4.12).

south of A98S are combined and shown in Figure 4.11. These box annuli are oriented to avoid the large-scale and intercluster filaments in the system. These values are then compared to the surface brightness in the apparent bridge regions connecting A98N and A98S shown in Figure 4.11.

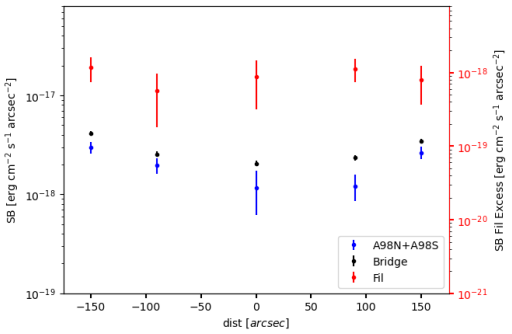

Figure 4.12: The surface brightness profile with XIS3 in the $0.5-2.0$ keV range, and 1σ errors for the filamentary region shown in Figure 4.11 is shown in black points, using the y-axis scale on the left. The corresponding combined rectangular annuli shown in Figure 4.11 for A98N and A98S are shown for comparison with the blue points. The filament excesses, are shown in red, using the y-axis scale on the right. The zero point on the x-axis is the midpoint of the tentative bridge connecting A98N to A98S.

The combined ICM surface brightness profile as compared to the bridge, and the resulting filament excess is presented in Figure 4.12 where the zero point on the x-axis is the midpoint of the region connecting A98N and A98S. The emission across the A98N-A98S bridge appears to be slightly enhanced, with a marginal

(2.2σ) detection of excess filament emission. This excess emission is also seen at a higher significance with combined *Suzaku* and deeper *Chandra* observations (Sarkar et al., 2022) than are presented in this paper.

4.2.2.2 Bridge Thermodynamic Properties

The temperature, electron density, entropy, and metallicity are measured across the A98 system with the box regions shown in e.g. Figure 3.5 (Right). The temperature profile from north to south is shown in Figure 4.13, and is relatively flat across A98N and A98S before dipping in between A98S and A98SS. When compared to *Chandra*, the temperature profiles are consistent.

In the intercluster region between A98N and A98S, a two temperature model is preferred (Table 4.3). The metallicity is frozen at its best fit value found from the one temperature fit, and the metallicity of the second temperature component is frozen to $Z = 0.2\ Z_{\odot}$.

Model	T_1 [keV]	T_2 [keV]	χ^2	d.o.f
1T APEC	$2.7^{+0.3}_{-0.2}$	-	267.3	225
2T APEC	$4.0^{+6.5}_{-1.0}$	$1.3^{+0.3}_{-0.3}$	249.9	224

Table 4.3: Parameters for a 1 temperature and 2 temperature model of the intercluster region between A98N and A98S.

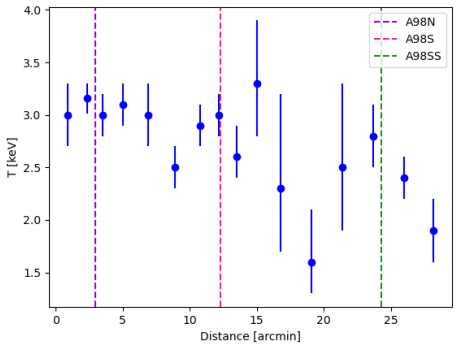

Figure 4.13: The temperature profile for the box regions across the A98 system shown in Figure 3.5. The profile starts from the north on the left of the plot. The purple, pink, and green dashed lines mark the center of A98N, A98S, and A98SS respectively.

The inferred electron density (Equation 4.1) for the regions across the bridge is presented in Figure 4.14. A cylindrical geometry is assumed for the regions in this profile. Assuming a box geometry for the regions across the bridge yields the same result within errors; therefore neither geometry is preferred. There is a steady decline in the electron density profile with local peaks corresponding to the cluster centers.

The metallicity profile across the bridge is shown in Figure 4.15. This profile suggests that the metallicity of the ICM is radius dependent, with a higher metallicity towards the center of the clusters, and decreases with radius.

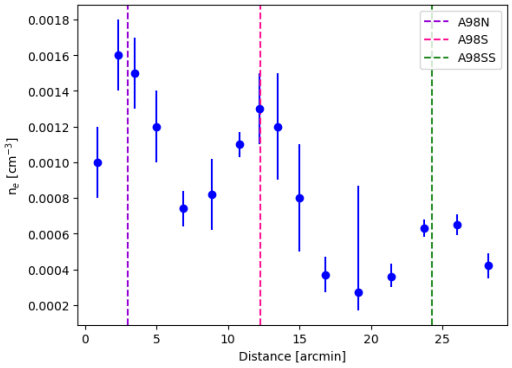

Figure 4.14: Inferred electron density profile across the A98 system. The profile is starting from the north on the left of the plot. The purple, pink, and green dashed lines mark the center of A98N, A98S, and A98SS respectively.

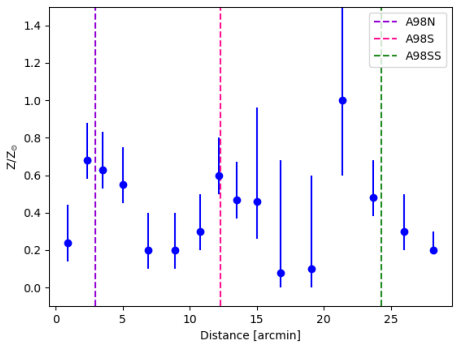

Figure 4.15: The metallicity profile across the A98 bridge. The profile is starting from the north on the left of the plot. The purple, pink, and green dashed lines mark the center of A98N, A98S, and A98SS respectively.

CHAPTER 5

Discussion and Conclusions

This chapter includes excerpts and figures from Alvarez et al. (2018) and Alvarez et al. (2022), used with permission from the Astrophysical Journal.

5.1 A3391/A3395 Discussion

5.1.1 The Filament

Here we discuss the derived density and entropy profiles, as well as the galaxy group ESO-161 to further explore the orientation and nature of the system.

5.1.1.1 Nature of the Filament

We fit the filament data with 2T models because there is likely contamination from ICM emission between r_{500}-r_{200}.. As shown in Chapter 3, we find that a 2T model is a better statistically significant fit for regions 2 and 3 with a cooler component ranging from $\sim 0.2-0.6$ keV (see Table 4.3). We find a group temperature of ~ 1.09 keV (see Section 5.1.2). We find that the measured cooler components in the filament regions are consistent with the temperature profile one would expect for an ~ 1 keV group at this distance from the group center based on the universal group temperature profile derived by Sun et al. (2009). Therefore, the 2T fits for both of the aforementioned regions as well as the box region shown in the right panel of Figure 3.5, which all cover r_{500} for the group, indicate that there is extended group emission in the filament beyond the group excluded region shown in Figure 3.5 (left panel).

The electron density (see Equation 4.1) profile for the filament, assuming it is in the plane of the sky, is shown in Figure 4.4. The black and cyan dashed lines are r_{200} for A3391 and A3395 respectively. There appears to be a dip in the electron density at the midpoint of the filament, at $\sim r_{200}$ of both the subclusters. This minimum in the density profile is approximately 2 dex higher than the mean baryonic density of the universe at the mean redshift of the system.

The entropy profile is shown in Figure 5.1 where we define entropy as $K = k_B T n_e^{-2/3}$, where k_b is Boltzmann's constant, n_e is the electron density, and T is the temperature. The entropy profiles for galaxy clusters derived from Voit et al. (2005) for A3391 and A3395 are shown in Figure 5.1, where the center of each cluster was determined from NED. The blue and green lines are the self-similar entropy profiles for A3391 and A3395 respectively:

$$K(r) = 1.41 \pm 0.03\, K_{200}\, (r/r_{200})^{1.1}. \tag{5.1}$$

K_{200} is the entropy at r_{200} and is defined as:

$$K_{200} = 362 \text{ keV cm}^2 \frac{\mathrm{T_X}}{1 \text{ keV}} \left(\frac{\mathrm{T_{200}}}{\mathrm{T_X}}\right) \times \left(\frac{\mathrm{H(z)}}{\mathrm{H_0}}\right)^{-4/3} \left(\frac{\Omega_\mathrm{m}}{0.3}\right)^{-4/3}, \tag{5.2}$$

where $T_X \approx T_{200}$, and Ω_m is the matter density parameter. The black vertical dashed line is r_{200} for A3391, and the cyan vertical dashed line is r_{200} for A3395. r_{200} values for the clusters were estimated using reported values of r_{500} (Piffaretti et al., 2011) and assuming $r_{200} \sim 1.7 r_{500}$ (e.g. AMI Consortium et al., 2012). We note that these values for r_{200} are slightly smaller than those reported in Sugawara et al. (2017). The values for r_{200} derived in Sugawara et al. (2017) are estimated using the empirical $r_{200} - T_X$ relation (Henry et al., 1981) and are 2.3 and 2.1 times the measured r_{500} value for A3391 and A3395 respectively. This difference in r_{200} affects the normalization of the self-similar entropy profile (see Section 5.1.1.2 for discussion).

The data points in Figure 5.1 represent the entropy derived from the measured 1T gas temperatures and electron densities shown in Figure 4.5 and Figure 4.4 respectively. The 90% temperature and electron density errors were propagated to derive the 90% entropy uncertainties (see Figure 5.1). The magenta pentagons are the entropy of the filament assuming it is in the plane of the sky ($i = 90°$) and the red triangles are entropy values for a filament orientation $i = 3.1°$ to the line of sight, the lowest inclination to the line of sight that Tittley and Henriksen (2001) argue for following their dynamical analysis of the system.

Even assuming the filament is in the plane of the sky, the entropy at large radii, namely near r_{200} for both clusters, is much larger than the expected entropy values for the dense range of the WHIM gas by at least a factor of four, with the predicted value for the WHIM at this redshift being approximately 250 keV cm^2 (Valageas et al., 2003).

All of the regions for the profile lie inside r_{200} of one, or both for the case of Region 4, of the subclusters. The extended ICM gas is expected to be hotter than the WHIM, and will bias the electron density towards higher values, so it is unclear what the overall entropy bias is due to these regions overlapping with the subcluster outskirts.

The radius of the filament profile geometry was assumed based upon the size of the *Chandra* observations, and the filament may actually be more extended than what is captured in the $16'$ by $16'$ observations. If this is the case, our electron density measurements are biased high. This in turn biases the entropy low, reinforcing the conclusion that the gas in the filamentary region is ICM gas, as the entropy across the filament is already too high to be consistent with the WHIM emission.

We find no evidence for a shock that would support the suggestion by Sugawara et al. (2017) of shock heated gas in this region. The flat temperature profile across the filament is consistent with ICM gas undergoing tidal pulling into the filament due to an early stage merger between the clusters. An interaction between

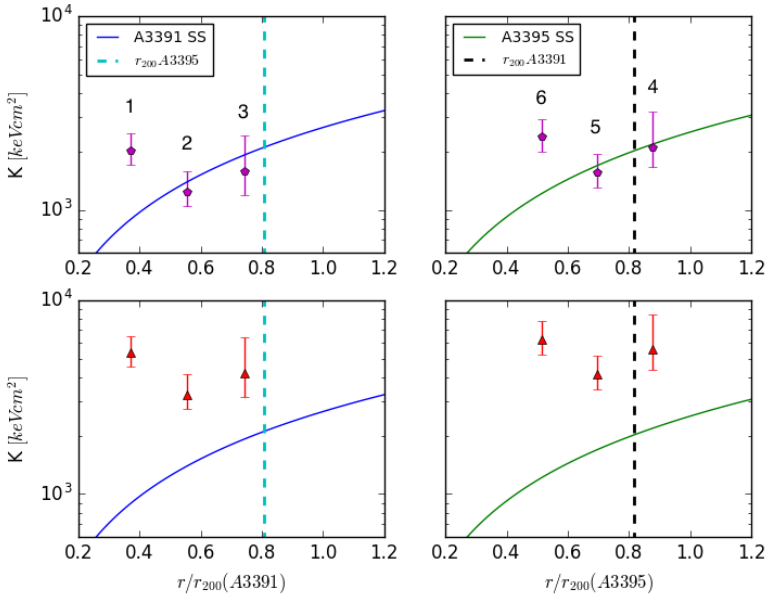

Figure 5.1: The blue line shows the self-similar entropy profile for A3391 derived from Voit et al. (2005) (left two panels). The green line is the same, but for A3395 (right two panels). The black vertical dashed line is r_{200} for A3391, and the cyan vertical dashed line is r_{200} for A3395. The data points are the derived entropy for the green box regions shown in the left panel of Figure 3.1 and points are labeled for reference. The magenta pentagons are the entropy, assuming the filament is in the plane of the sky, and the red triangles are entropy values for a filament orientation i = 3.1° to the line of sight, as suggested by Tittley and Henriksen (2001). The distance shown on the x-axis is the distance from the cluster center.

the subclusters was also recently suggested by Sugawara et al. (2017).

5.1.1.2 Orientation of the Filament

It has been shown that the entropy profile of most massive clusters lies at about self-similar within r_{500}, and then flattens below self-similar at larger radii (i.e. Walker et al., 2013). There is an uncertainty when relating a measured r_{500} with r_{200}. The effect that this has on the self-similar entropy profile is in the normalization of the profile. This uncertainty in the normalization of the self-similar entropy profile makes it difficult to say with conviction which inclination brings the profile closer to an expected self-similar value. Figure 5.1 suggests a filamentary geometry close to the plane of the sky. The larger r_{200} values determined empirically by Sugawara et al. (2017) only serve to strengthen the argument for a filament orientation closer to the plane of the sky than the range close to the plane of the sky reported in other works, as the larger r_{200} values decrease the normalization of the self-similar entropy profile. In any case, this uncertainty in normalization does not change the observed flattening of the entropy profile.

Given that the global filamentary temperature is ~ 4.5 keV, the gas is very likely from the ICM outskirts of the two clusters, in which case the clusters must be close enough to be tidally interacting and cannot have a large line-of-sight separation.

Tittley and Henriksen (2001) found through a dynamical analysis of the system that the subclusters and the connecting filament are oriented close to the line of sight, having an inclination, i, between $3.1^\circ - 9.0^\circ$. Sugawara et al. (2017) suggest that the filament may be inclined $\approx 10^\circ$ to the line of sight in order for their X-ray measured Compton y parameter to agree with the y_{SZ} parameter reported by Planck Collaboration et al. (2013) for the filament. However, Sugawara et al. (2017) also suggest that the discrepancy in y parameters is likely a combination of the system not being in the plane of the sky, or there is unresolved multi-phase gas or shock heated gas present in the *Suzaku* observations. Indeed, if the system is inclined 10° to the line of sight, the true separation between the subclusters would be over 17 Mpc, making it unlikely for the clusters to be interacting. However, we note that the center of the galaxy group ESO-161 is just outside the *Suzaku* field of view, so the extended cooler phase gas from the group, mixing with the surrounding filament gas may be an explanation for the y parameter discrepancy.

The line of sight velocity difference of the clusters (~ 240 km s^{-1} (Struble and Rood, 1999)) is rather small and consistent with an early stage merger without a large line-of-sight peculiar velocity component. If the velocity difference were much larger then that would imply the clusters are significantly unbound and unable to interact tidally, or that the clusters are undergoing a late stage merger. The former scenario is in contradiction with the temperature and entropy values that we measure, and the latter scenario contradicts the observed line of sight separation between the clusters.

5.1.2 ESO-161

To constrain the temperature of the galaxy group ESO-161, we fit the group region (see the left panel of Figure 3.1) with an absorbed APEC model and the same background prescription described in Chapter 3; we use the dashed circular region to the east of the group shown in the left panel of Figure 3.1 to simultaneously model the local background. Our fit yielded a temperature of $1.09^{+0.58}_{-0.05}$keV for the group. This temperature is significantly cooler than the best fit for the surrounding region, $4.45^{+0.89}_{-0.55}$ keV (see Chapter 4).

The emission to the west of the group (see Figure 3.3) is indicative of a diffuse tail. With *Chandra*, this diffuse gas can be resolved into a bimodal structure (see Figure 4.2). We use the azimuthal regions shown in Figure 4.2 to derive the azimuthal surface brightness profile in the 0.3-3.0 keV band shown in Figure 5.2. This profile shows a hint of a double peak, in the same position as the arrows pointing towards the ram pressure stripped tail candidates (see the right panel of Figure 4.2) indicated by the dotted lines, furthering evidence that the tail indeed may have a bimodal structure. The extended emission to the west of ESO-161 is suggestive that the group may be undergoing ram pressure stripping as the group moves through the filament.

The bimodal tail may have a "downstream edge" to the west of the group center, which is more apparent in the right panel of Figure 4.1. This bimodal tail structure may indicate an ellipsoidal potential in origin (e.g. Roediger et al., 2015) for the group. Randall et al. (2008) first suggested that the double tails are due to stripping from ellipsoidal potentials.

Another clue bolstering the ram pressure stripping scenario is the possible cold front shown in Figure 4.1. The northeastern edge is consistent with the "upstream edge" reported in Roediger et al. (2015) for systems experiencing ram pressure stripping as they move through an ambient medium.

To further investigate the prominent edge seen to the east of the galaxy group in Figure 4.1, we derived a surface brightness profile in the northeast region of the group shown in Figure 4.2 (left panel), which may be seen in Figure 5.3.

There is a clear drop in surface brightness at $\sim 2'$ in Figure 5.3, moving radially away from the group. We do not have enough data to distinguish if this edge is really a cold front, shock front, or neither. More observing time with *XMM-Newton* would shed light on this question. This apparent edge, as well as the bimodal tail structure of stripped gas is indicative that the galaxy group is consistent with moving east in projection through the filament.

Gunn and Gott (1972) give the conditions for ram pressure stripping to occur as $P_{ram} = \frac{1}{2}\rho_{ICM} v_r^2 \gtrsim \sigma^2 \rho_{gas}$, where ρ_{ICM} is the density of the intercluster medium, v_r is the velocity of the group relative to the intercluster medium, P_{ram} is the ram pressure, σ is the galaxy group's velocity dispersion, and ρ_{gas} is the group's gas density. In order to estimate the gas density of the group, we assume an oblate spheroid geometry, with the

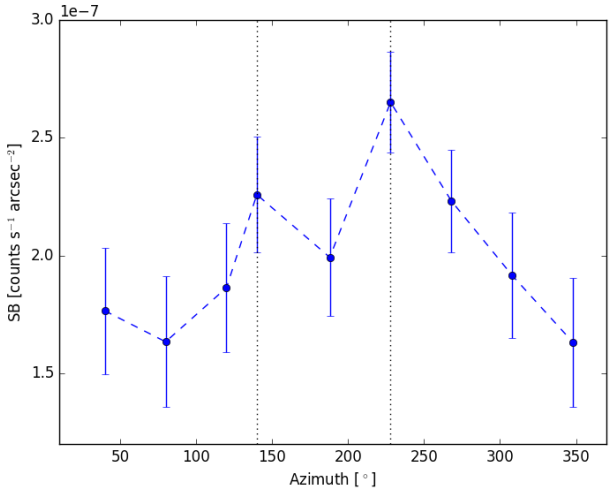

Figure 5.2: The surface brightness profile for the azimuthal regions shown in Figure 4.2 in the 0.3-3.0 keV band. The dotted lines indicate the position of the arrows in Figure 4.2, pointing towards the visual stripped tails of gas. Errors are 1σ.

line-of-sight axis equal to the projected major axis and the minor axis in the plane of the sky. Using the electron density inferred from the box region in Figure 3.1 (right panel), the density for the group region is $n_e \sim 1.8 \times 10^{-4}$ cm^{-3}. Tittley and Henriksen (2001) report that the group velocity dispersion is 1800 km/s. This velocity dispersion is much too high for the group to be bound, so we use the following method to roughly estimate the velocity dispersion of ESO-161.

We use the $M_x - T_x$ relation derived by Vikhlinin et al. (2009) to estimate M_{500}. While the sample used to derive the $M_x - T_x$ relation in Vikhlinin et al. (2009) consists of galaxy clusters and not groups, Sun et al. (2009) report that the relation also holds for lower temperature galaxy clusters and groups. We find that $M_{500} \sim 2.3 \times 10^{13}$ M$_\odot$. Assuming spherical symmetry we may then use $M_{500} = 500 \times \rho_c \frac{4}{3} \pi r_{500}^3$, where ρ_c is the critical density of the Universe at the redshift of ESO-161, 9.86×10^{-30} g cm^{-3}, and r_{500} is the radius at which the density of the galaxy group is 500 times the critical density of the Universe at the redshift of

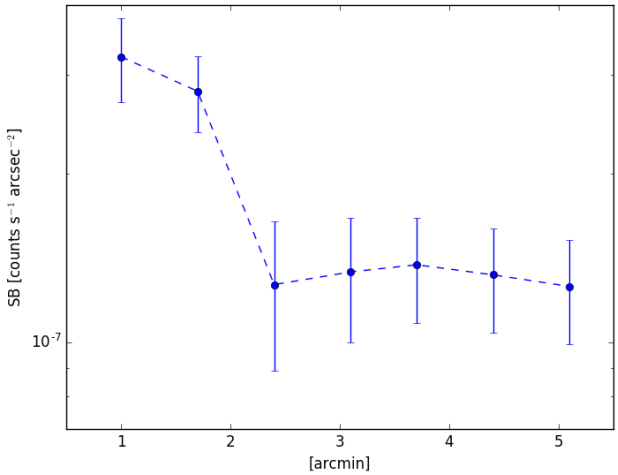

Figure 5.3: The *Chandra* surface brightness profile in the 0.3-3.0 keV band for the region shown in the left panel of Figure 4.2, centered on the group. Errors are 1σ.

the galaxy group, to estimate the radius of the group. Finally, we may then use $M_{500} = \frac{3}{G}\sigma^2 r_{500}$, where G is the gravitational constant and σ is the velocity dispersion of the group. We find that the group has a velocity dispersion of ~ 250 km s^{-1}. This velocity dispersion is approximately six times lower than what Tittley and Henriksen (2001) report.

We find that the group must have a relative velocity to the filamentary region $v_r \geq 360$ km s^{-1} in order for ram pressure stripping to occur. If the filament is oriented to the median inclination angle given by Tittley and Henriksen (2001), then the minimum relative velocity would have to be ~ 630 km/s as the group moves eastward through the filament.

Another possibility for the extended emission to the west of the group is tidal stripping, perhaps due to a gravitational interaction with another massive object. The extended emission to the north of the group (see the right panel of Figure 4.1), as well as the <1 keV temperatures found in regions to the north of the group (see Table 4.3) could indicate that ESO-161 is moving to the southeast, around A3391, and the group experienced a tidal stripping event. The emission to the west may also be the result of tidal stripping due to an interaction with a currently unidentified, possibly gas stripped object.

In any case, these gaseous double tail-like structures are commonly seen in ram pressure stripped galaxies, most notably in the Virgo Cluster (i.e. Forman et al., 1979; Randall et al., 2008), and in simulations (i.e. Roediger et al., 2015). This would therefore lead to the conclusion that ESO-161 is being ram pressure stripped as it moves eastward in projection through the intercluster filament. We note that such clear examples of ram pressure stripped galaxy groups near low density cluster outskirt environments are quite rare (e.g. De Grandi et al., 2016).

5.2 A98 Discussion

5.2.1 Large-Scale Filament

The box region to the north of A98N shown in Figure 3.5 Left is used to investigate larger-scale structure beyond r_{200} of A98N. The excluded region within the box does not appear to be a point source, and also does not appear to be associated with the A98 system. Inspecting images from the DSS and SDSS reveals no obvious clustering of galaxies. There are not enough photons available to reliably model the spectrum of this source. This source could be a background galaxy cluster or faint group, although it would require further observations to determine its nature. A 1D-β model is fit to the circular region encompassing the possible background cluster, with best fit parameters $\beta \approx 1.3$ and $r_c \approx 2'$. This model is extrapolated to compare the expected surface brightness, to the measured surface brightness in the rest of the box region shown in Figure 3.5 Left. The measured surface brightness is larger than the expected surface brightness by approximately a factor of 4.

This region was fitted with an absorbed APEC model. The best fit values for this box region, excluding the possible background cluster, yield a projected temperature of $kT = 0.11^{+0.01}_{-0.02}$ keV, projected electron density $n_e = 7.6 \times 10^{-5}{}^{+3.6\times10^{-5}}_{-3.6\times10^{-5}}$ cm^{-3}, and a projected entropy K = 61^{+20}_{-22} keV cm^2 assuming a cylindrical volume with length $l = 0.62$ Mpc and radius of $r = 0.61$ Mpc, and filling factor of 1 for the density measurement. These values are consistent with the dense end of the WHIM, where the ICM in the outskirts of the cluster interact with the large-scale structure filament (e.g. Dolag et al., 2006; Werner et al., 2008), especially if the system is not oriented in the plane of the sky.

We compare a similar region to the west, and fit the region with the best fit parameters for the model of the northern region. The fit for the northern box region yields a χ^2 of 289.24 with 272 d.o.f. We find that the western comparison region is consistent with background only with a fit that gives a χ^2 of 555.21 with 321 d.o.f when the data is fit to the best fit model of the northern region. Additionally, this region is fit with a background only model for comparison. The model with the extra apec component (χ^2/d.o.f = 289.25/273) is favored ($p = 0.06$) over the background only model (χ^2/d.o.f = 293/274). Such detections of this material are very rare (e.g. Bulbul et al., 2016; Werner et al., 2008). This detection is consistent with the detection of larger-scale structure in the Abell 1750 system, another low mass triple cluster system (Bulbul et al., 2016) similar to A98. With the advent of *eRosita* and future X-ray missions (e.g. *Athena, Lynx*), such detections should become more common.

5.2.1.1 Filament Orientation

The cyan box regions shown in e.g. Figure 3.5 (Right) between A98N and A98S can be used to explore the entropy, presumed geometry, and inclination of the system. The entropy profile for the box regions between A98N and A98S is shown in Figure 5.4. We only include the regions from the center of A98N to the center of A98S in this entropy profile to investigate the filament orientation (cyan regions in e.g. Figure 3.5 (Right)).

The two extremes for filament orientation: along the line of sight (los) and in the plane of the sky (pos) are investigated (see Figure 5.4). At the midpoint of the filament, the measured entropy is already approximately the expected ICM value at this radius if the filament is in the pos. This means that either the filament is in the pos, or the entropy of the gas has somehow been increased (e.g., due to a merger shock (Sarkar et al., 2022)). The filament is more likely inclined close to the pos, as a los filament orientation yields entropy values well above what is expected from the self-similar entropy profiles of the clusters (Voit et al., 2005). Furthermore, a line of sight orientation of the system yields entropy values ~ 2 times higher than what is expected in the outskirts of both subclusters. These measurements rule out a significant contribution from WHIM emission in this region. The reported entropy values similarly assume a cylindrical geometry for the bridge regions, and assuming a box geometry yields a similar result within errors.

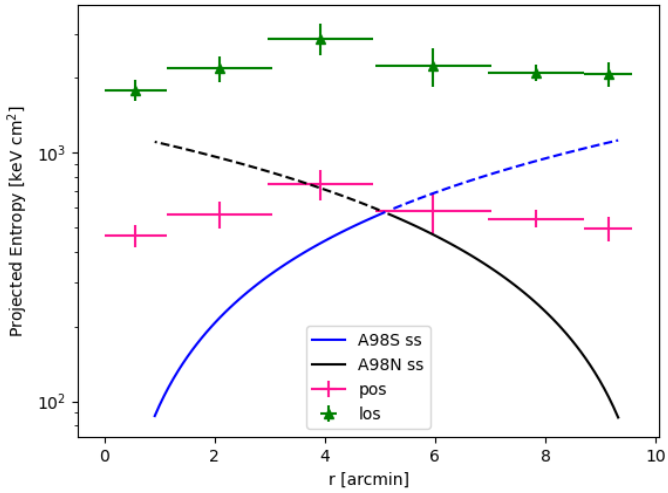

Figure 5.4: The entropy profile from north to south across the bridge between A98N and A98S. The blue line is the expected universal entropy profile for A98N. The black line is the expected universal entropy profile for A98S. The pink points are the inferred entropy for a filament orientation in the pos. The green triangles are for a filament orientation along the los. A filament orientation closer to the pos is preferred, as the los entropy values are ~ 2 times higher than what is expected in the outskirts of both subclusters.

This section will describe the findings for the temperature structure around A98N with *Suzaku*.

5.3 Conclusions

In these studies, a picture similar to the large-scale structure seen in cosmological simulations starts to emerge. *Suzaku* is a powerful tool for studying diffuse ICM emission at large cluster radii, but is no longer functional and available for future observations. The diffuse and low-surface brightness emission explored in this work already pushes *Chandra* and XMM-*Newton* to their limits, and these instruments and their effective area continue to age and degrade.

The next generation of X-ray telescopes such as *eRosita, XRISM, Athena*, and *Lynx* will provide a wealth of information on the diffuse ICM in the virialization region of galaxy clusters and the surrounding large-scale structure (e.g. Reiprich et al., 2021). The ability to study increasingly low surface brightness cluster outskirt emission will help to answer key questions about the physical processes occurring in these interface regions. This will lead to a new era of synergy between observation and simulation in the pursuit to understand cosmology and the physics that govern the observable Universe. Presented here are the conclusions and summary for this work.

5.3.1 A3391/A3395 Conclusions

The results based on *Chandra* and XMM-*Newton* observations of the intercluster gas filament connecting A3391 and A3395 are presented. The following is found:

- A global projected temperature kT = $4.45^{+0.89}_{-0.55}$ keV, electron density $n_e = 1.08^{+0.06}_{-0.05} \times 10^{-4} \sin(i)^{\frac{1}{2}}$ cm^{-3} for the intercluster filament.
- The temperature and electron density derived for the global intercluster filamentary region indicates that the filament gas mass is $M_{\rm gas} = 2.7^{+0.2}_{-0.1} \times 10^{13} \sin(i)^{-\frac{1}{2}}$ M$_\odot$. This is a similar mass to what is reported for the intercluster filament between the two subclusters Abell 222 and Abell 223 (Werner et al., 2008), and is consistent with what Tittley and Henriksen (2001) found in their analysis with *ROSAT* for A3395/A3391.
- The temperature and entropy profiles derived for the filament suggest ICM gas is being tidally pulled into the intercluster filamentary region as part of an early stage pre-merger. The density across the intercluster filament is consistent with the dense WHIM as well as what is expected in cluster outskirts, near the virial radius, although the temperature and entropy are much higher than what is expected for the WHIM.
- The galaxy group ESO-161, located between A3391 and A3395 in the intercluster filament, may be undergoing a stripping event as the group moves eastward seemingly perpendicular to the filament with a minimum relative velocity of approximately 360 km s^{-1} if the filament is oriented in the plane of the sky. In addition, the group has a distinct edge in surface brightness to the east, which would require a deeper observation with XMM-*Newton* to characterize.

Since the subclusters appear to be tidally interacting, their line of sight separation must not be large, leading us to conclude that the filament is probably not oriented close to the line of sight as was suggested by Tittley and Henriksen (2001).

The only evidence we find for cooler phase gas is that likely associated with the galaxy group ESO-161, however the WHIM cannot be ruled out. The filament density, even in projection, is consistent with the theoretical density of the WHIM, however this density is also consistent with density profiles of clusters out to the virial radius (Morandi et al., 2015).

Sugawara et al. (2017) argue that the filament temperature is too high to be explained by universal cluster temperature profiles of the subclusters, and attribute this to a shock, perhaps as the subclusters merge. We do not find evidence for merger shocks in the filament. The 4.5 keV filament temperature that we measure is consistent with ICM gas being tidally pulled into the intercluster filament in the early stages of a massive

cluster merger. This heated gas above the cluster temperature profiles as well as temperatures expected for the WHIM could also be attributed to adiabatic compression in the filament.

5.3.2 A98 Conclusions

In this thesis the results from an analysis of *Suzaku, Chandra* and XMM-*Newton* observations of the diffuse emission in the A98 system are presented.

We find the following:

- The entropy profiles in northern and western sectors, along and away from the merger axis and the putative large scale structure filament, for A98N generally agree with each other, and with the self-similar expectation in the virialization region. This is consistent with previous suggestions (e.g. Su et al., 2015; Bulbul et al., 2016) that lower mass clusters and groups adhere more closely to self-similar expectations in their outskirts, in contrast with what is seen in most massive systems.

- The region to the north of A98N, beyond r_{200}, was found to have a temperature, density, and entropy consistent with those expected for the dense end of the WHIM. We find a temperature of $kT = 0.11^{+0.01}_{-0.02}$ keV, projected electron density $n_e = 7.6 \times 10^{-5}{}^{+3.6\times10^{-5}}_{-3.6\times10^{-5}}$ cm^{-3}, and a projected entropy $K = 61^{+20}_{-22}$ keV cm^2 for this region. The presence of similar emission at the same radius to the west, away from the putative large scale structure filament, is ruled out. This serves as further evidence that the system is consistent with the expectation that the merger axis lies along a large-scale structure filament. A similar result was found in the colinear triple system Abell 1750 (Bulbul et al., 2016). These measurements provide tantalizing evidence for the presence of a larger-scale structure, with the diffuse WHIM connecting to the cluster outskirts along cosmic filaments.

- When comparing the surface brightness of the A98N- A98S bridge regions to the combined surface brightness profiles of the two overlapping halos, a nominal 2.2σ excess in bridge emission is detected. This detection is suggestive of the presence of an intercluster filament in-between the two clusters. Additionally, there is evidence of two-phase plasma in this region; the lower temperature component ($kT \sim 1$ keV) is consistent with the dense end of the WHIM.

- Comparing the entropy profile of the A98N-A98S bridge to that of the self-similar expectations for A98N and A98S reveals that the system is likely inclined closer to the pos. This suggests that the clusters are interacting with each other as they are well within each other's virial radius in projection.

References

Abell, G. O. (1957). The distribution of rich clusters of galaxies. *AJ*, 62:2.

Abell, G. O., Corwin, Harold G., J., and Olowin, R. P. (1989). A Catalog of Rich Clusters of Galaxies. *ApJS*, 70:1.

Allen, S. W. and Fabian, A. C. (1998). The impact of cooling flows on the T_X-L_Bol relation for the most luminous clusters. *MNRAS*, 297:L57–L62.

Alvarez, G. et al. (2022). *Suzaku* observations of the cluster outskirts and intercluster filament in the triple merger cluster abell 98.

Alvarez, G. E., Randall, S. W., Bourdin, H., Jones, C., and Holley-Bockelmann, K. (2018). Chandra and XMM-Newton Observations of the Abell 3395/Abell 3391 Intercluster Filament. *ApJ*, 858(1):44.

AMI Consortium, Rodríguez-Gonzálvez, C., Shimwell, T. W., Davies, M. L., Feroz, F., Franzen, T. M. O., Grainge, K. J. B., Hobson, M. P., Hurley-Walker, N., Lasenby, A. N., Olamaie, M., Pooley, G., Saunders, R. D. E., Scaife, A. M. M., Schammel, M. P., Scott, P. F., Titterington, D. J., and Waldram, E. M. (2012). Detailed Sunyaev-Zel'dovich study with AMI of 19 LoCuSS galaxy clusters: masses and temperatures out to the virial radius. *MNRAS*, 425:162–203.

Angelinelli, M., Ettori, S., Vazza, F., and Jones, T. W. (2021). Properties of clumps and filaments around galaxy clusters. *arXiv e-prints*, page arXiv:2102.01096.

Arnaud, M. and Evrard, A. E. (1999). The L_X-T relation and intracluster gas fractions of X-ray clusters. *MNRAS*, 305:631–640.

Avestruz, C., Nagai, D., Lau, E. T., and Nelson, K. (2015). Non-equilibrium Electrons in the Outskirts of Galaxy Clusters. *ApJ*, 808:176.

Battaglia, N., Bond, J. R., Pfrommer, C., and Sievers, J. L. (2013). On the Cluster Physics of Sunyaev-Zel'dovich and X-Ray Surveys. III. Measurement Biases and Cosmological Evolution of Gas and Stellar Mass Fractions. *ApJ*, 777:123.

Bautz, M. W., Miller, E. D., Sanders, J. S., Arnaud, K. A., Mushotzky, R. F., Porter, F. S., Hayashida, K., Henry, J. P., Hughes, J. P., Kawaharada, M., Makashima, K., Sato, M., and Tamura, T. (2009). Suzaku Observations of Abell 1795: Cluster Emission to r_{200}. *PASJ*, 61:1117–1133.

Bennett, C. L., Larson, D., Weiland, J. L., Jarosik, N., Hinshaw, G., Odegard, N., Smith, K. M., Hill, R. S., Gold, B., Halpern, M., Komatsu, E., Nolta, M. R., Page, L., Spergel, D. N., Wollack, E., Dunkley, J., Kogut, A., Limon, M., Meyer, S. S., Tucker, G. S., and Wright, E. L. (2013). Nine-year Wilkinson Microwave Anisotropy Probe (WMAP) Observations: Final Maps and Results. *ApJs*, 208(2):20.

Bourdin, H., Bijaoui, A., Sauvageot, J.-L., Belsole, E., and Slezak, E. (2005). Wavelet mapping of the intra-cluster medium emissivity and temperature structures within clusters of galaxies observed by XMM-Newton. *Advances in Space Research*, 36:650–655.

Bourdin, H. and Mazzotta, P. (2008). Temperature structure of the intergalactic medium within seven nearby and bright clusters of galaxies observed with XMM-Newton. *A&A*, 479:307–320.

Bourdin, H., Mazzotta, P., Markevitch, M., Giacintucci, S., and Brunetti, G. (2013). Shock Heating of the Merging Galaxy Cluster A521. *ApJ*, 764:82.

Bregman, J. N. (2007). The Search for the Missing Baryons at Low Redshift. *AARA*, 45:221–259.

Bulbul, E., Randall, S. W., Bayliss, M., Miller, E., Andrade-Santos, F., Johnson, R., Bautz, M., Blanton, E. L., Forman, W. R., Jones, C., Paterno-Mahler, R., Murray, S. S., Sarazin, C. L., Smith, R. K., and Ezer, C. (2016). Probing the Outskirts of the Early-Stage Galaxy Cluster Merger A1750. *ApJ*, 818:131.

Burns, J. O., Rhee, G., Owen, F. N., and Pinkney, J. (1994). Clumped X-Ray Emission around Radio Galaxies in Abell Clusters. *ApJ*, 423:94.

Candès, E. J. and Donoho, D. L. (2002). Recovering edges in ill-posed inverse problems: optimality of curvelet frames. *Ann. Statist.*, 30(3):784–842.

Cen, R. and Ostriker, J. P. (1999). Where Are the Baryons? *ApJ*, 514:1–6.

Davé, R., Cen, R., Ostriker, J. P., Bryan, G. L., Hernquist, L., Katz, N., Weinberg, D. H., Norman, M. L., and O'Shea, B. (2001). Baryons in the Warm-Hot Intergalactic Medium. *ApJ*, 552:473–483.

David, L. P., Jones, C., and Forman, W. (1995). Cosmological implications of ROSAT observations of groups and clusters of galaxies. *ApJ*, 445:578–590.

de Graaff, A., Cai, Y.-C., Heymans, C., and Peacock, J. A. (2017). Missing baryons in the cosmic web revealed by the Sunyaev-Zel'dovich effect. *ArXiv e-prints*.

De Grandi, S., Eckert, D., Molendi, S., Girardi, M., Roediger, E., Gaspari, M., Gastaldello, F., Ghizzardi, S., Nonino, M., and Rossetti, M. (2016). A textbook example of ram-pressure stripping in the Hydra A/A780 cluster. *A&A*, 592:A154.

Dolag, K., Meneghetti, M., Moscardini, L., Rasia, E., and Bonaldi, A. (2006). Simulating the physical properties of dark matter and gas inside the cosmic web. *MNRAS*, 370(2):656–672.

Eckert, D., Roncarelli, M., Ettori, S., Molendi, S., Vazza, F., Gastaldello, F., and Rossetti, M. (2015). Gas clumping in galaxy clusters. *MNRAS*, 447(3):2198–2208.

Edge, A. C. and Stewart, G. C. (1991). EXOSAT observations of clusters of galaxies. I - The X-ray data. II - X-ray to optical correlations. *MNRAS*, 252:414–441.

Ettori, S., Gastaldello, F., Leccardi, A., Molendi, S., Rossetti, M., Buote, D., and Meneghetti, M. (2010). Mass profiles and c-M_{DM} relation in X-ray luminous galaxy clusters. *A&A*, 524:A68.

Fang, T., Canizares, C. R., and Yao, Y. (2007). Confirming the Detection of an Intergalactic X-Ray Absorber toward PKS 2155-304. *ApJ*, 670:992–999.

Forman, W., Bechtold, J., Blair, W., Giacconi, R., van Speybroeck, L., and Jones, C. (1981). Einstein imaging observations of clusters with a bimodal mass distribution. *ApJl*, 243:L133–L136.

Forman, W., Schwarz, J., Jones, C., Liller, W., and Fabian, A. C. (1979). X-ray observations of galaxies in the Virgo cluster. *ApJl*, 234:L27–L31.

Fox, D. C. and Loeb, A. (1997). Do the Electrons and Ions in X-Ray Clusters Share the Same Temperature? *ApJ*, 491:459–466.

Fukugita, M., Hogan, C. J., and Peebles, P. J. E. (1998). The Cosmic Baryon Budget. *ApJ*, 503:518–530.

Ghirardini, V., Eckert, D., Ettori, S., Pointecouteau, E., Molendi, S., Gaspari, M., Rossetti, M., De Grandi, S., Roncarelli, M., Bourdin, H., Mazzotta, P., Rasia, E., and Vazza, F. (2019). Universal thermodynamic properties of the intracluster medium over two decades in radius in the X-COP sample. *A&A*, 621:A41.

Giodini, S., Lovisari, L., Pointecouteau, E., Ettori, S., Reiprich, T. H., and Hoekstra, H. (2013). Scaling Relations for Galaxy Clusters: Properties and Evolution. *SSRv*, 177(1-4):247–282.

González, R. E. and Padilla, N. D. (2009). Galaxy star formation in different environments. *MNRAS*, 397:1498–1509.

Grevesse, N. and Sauval, A. J. (1998). Standard Solar Composition. *SSR*, 85:161–174.

Gunn, J. E. and Gott, III, J. R. (1972). On the Infall of Matter Into Clusters of Galaxies and Some Effects on Their Evolution. *ApJ*, 176:1.

Heitmann, K., Frontiere, N., Rangel, E., Larsen, P., Pope, A., Sultan, I., Uram, T., Habib, S., Finkel, H., Korytov, D., Kovacs, E., Rizzi, S., Insley, J., and Knowles, J. Y. K. (2021). The Last Journey. I. An Extreme-scale Simulation on the Mira Supercomputer. *ApJs*, 252(2):19.

Henry, J. P., Henriksen, M. J., Charles, P. A., and Thorstensen, J. R. (1981). Observations of the two components of the Abell 98 cluster of galaxies. *ApJl*, 243:L137–L142.

Hickox, R. C. and Markevitch, M. (2006). Absolute Measurement of the Unresolved Cosmic X-Ray Background in the 0.5-8 keV Band with Chandra. *ApJ*, 645:95–114.

Hirata, C. and Seljak, U. (2003). Shear calibration biases in weak-lensing surveys. *MNRAS*, 343(2):459–480.

Hoshino, A., Henry, J. P., Sato, K., Akamatsu, H., Yokota, W., Sasaki, S., Ishisaki, Y., Ohashi, T., Bautz, M., Fukazawa, Y., Kawano, N., Furuzawa, A., Hayashida, K., Tawa, N., Hughes, J. P., Kokubun, M., and Tamura, T. (2010). X-Ray Temperature and Mass Measurements to the Virial Radius of Abell 1413 with Suzaku. *PASJ*, 62:371–389.

Ichikawa, K., Matsushita, K., Okabe, N., Sato, K., Zhang, Y.-Y., Finoguenov, A., Fujita, Y., Fukazawa, Y., Kawaharada, M., Nakazawa, K., Ohashi, T., Ota, N., Takizawa, M., Tamura, T., and Umetsu, K. (2013). Suzaku Observations of the Outskirts of A1835: Deviation from Hydrostatic Equilibrium. *ApJ*, 766:90.

Ikebe, Y., Reiprich, T. H., Böhringer, H., Tanaka, Y., and Kitayama, T. (2002). A new measurement of the X-ray temperature function of clusters of galaxies. *A&A*, 383:773–790.

Jones, C. and Forman, W. (1999). Einstein Observatory Images of Clusters of Galaxies. *ApJ*, 511(1):65–83.

Kaiser, N. (1986). Evolution and clustering of rich clusters. *MNRAS*, 222:323–345.

Kalberla, P. M. W., Burton, W. B., Hartmann, D., Arnal, E. M., Bajaja, E., Morras, R., and Pöppel, W. G. L. (2005). The Leiden/Argentine/Bonn (LAB) Survey of Galactic HI. Final data release of the combined LDS and IAR surveys with improved stray-radiation corrections. *A&A*, 440:775–782.

Kaplinghat, M. and Turner, M. S. (2001). Precision Cosmology and the Density of Baryons in the Universe. *Physical Review Letters*, 86:385–388.

Kauffmann, G., Colberg, J. M., Diaferio, A., and White, S. D. M. (1999). Clustering of galaxies in a hierarchical universe - I. Methods and results at z=0. *MNRAS*, 303(1):188–206.

Köhlinger, F., Hoekstra, H., and Eriksen, M. (2015). Statistical uncertainties and systematic errors in weak lensing mass estimates of galaxy clusters. *MNRAS*, 453(3):3107–3119.

Kull, A. and Böhringer, H. (1999). Detection of filamentary X-ray structure in the core of the Shapley supercluster. *A&A*, 341:23–28.

Kuntz, K. D. and Snowden, S. L. (2000). Deconstructing the Spectrum of the Soft X-Ray Background. *ApJ*, 543:195–215.

Kuntz, K. D. and Snowden, S. L. (2008). The EPIC-MOS particle-induced background spectra. *A&A*, 478:575–596.

Lau, E. T., Kravtsov, A. V., and Nagai, D. (2009). Residual Gas Motions in the Intracluster Medium and Bias in Hydrostatic Measurements of Mass Profiles of Clusters. *ApJ*, 705:1129–1138.

Lovisari, L., Reiprich, T. H., and Schellenberger, G. (2015). Scaling properties of a complete X-ray selected galaxy group sample. *A&A*, 573:A118.

Markevitch, M. and Vikhlinin, A. (2007). Shocks and cold fronts in galaxy clusters. *PhysRep*, 443(1):1–53.

Massey, R., Hoekstra, H., Kitching, T., Rhodes, J., Cropper, M., Amiaux, J., Harvey, D., Mellier, Y., Meneghetti, M., Miller, L., Paulin-Henriksson, S., Pires, S., Scaramella, R., and Schrabback, T. (2013). Origins of weak lensing systematics, and requirements on future instrumentation (or knowledge of instrumentation). *MNRAS*, 429(1):661–678.

Mirakhor, M. S. and Walker, S. A. (2020). A complete view of the outskirts of the Coma cluster. *MNRAS*, 497(3):3204–3220.

Morandi, A., Sun, M., Forman, W., and Jones, C. (2015). The galaxy cluster outskirts probed by Chandra. *MNRAS*, 450:2261–2278.

Moretti, A., Campana, S., Lazzati, D., and Tagliaferri, G. (2003). The Resolved Fraction of the Cosmic X-Ray Background. *ApJ*, 588:696–703.

Nelson, D., Springel, V., Pillepich, A., Rodriguez-Gomez, V., Torrey, P., Genel, S., Vogelsberger, M., Pakmor, R., Marinacci, F., Weinberger, R., Kelley, L., Lovell, M., Diemer, B., and Hernquist, L. (2019). The IllustrisTNG simulations: public data release. *Computational Astrophysics and Cosmology*, 6(1):2.

Nicastro, F., Kaastra, J., Krongold, Y., Borgani, S., Branchini, E., Cen, R., Dadina, M., Danforth, C. W., Elvis, M., Fiore, F., Gupta, A., Mathur, S., Mayya, D., Paerels, F., Piro, L., Rosa-Gonzalez, D., Schaye, J., Shull, J. M., Torres-Zafra, J., Wijers, N., and Zappacosta, L. (2018). Observations of the missing baryons in the warm-hot intergalactic medium. *NAT*, 558(7710):406–409.

O'Sullivan, E., Giacintucci, S., David, L. P., Gitti, M., Vrtilek, J. M., Raychaudhury, S., and Ponman, T. J. (2011). Heating the Hot Atmospheres of Galaxy Groups and Clusters with Cavities: The Relationship between Jet Power and Low-frequency Radio Emission. *ApJ*, 735(1):11.

Paterno-Mahler, R., Randall, S. W., Bulbul, E., Andrade-Santos, F., Blanton, E. L., Jones, C., Murray, S., and Johnson, R. E. (2014). Merger Signatures in the Galaxy Cluster A98. *ApJ*, 791(2):104.

Paul, S., John, R. S., Gupta, P., and Kumar, H. (2017). Understanding 'galaxy groups' as a unique structure in the universe. *MNRAS*, 471(1):2–11.

Piffaretti, R., Arnaud, M., Pratt, G. W., Pointecouteau, E., and Melin, J.-B. (2011). The MCXC: a meta-catalogue of x-ray detected clusters of galaxies. *A&A*, 534:A109.

Pinkney, J., Burns, J. O., Ledlow, M. J., Gómez, P. L., and Hill, J. M. (2000). Substructure in Clusters Containing Wide-Angle-Tailed Radio Galaxies. I. New Redshifts. *AJ*, 120(5):2269–2277.

Planck Collaboration, Ade, P. A. R., Aghanim, N., Akrami, Y., Aluri, P. K., Arnaud, M., Ashdown, M., Aumont, J., Baccigalupi, C., Banday, A. J., Barreiro, R. B., Bartolo, N., Basak, S., Battaner, E., Benabed, K., Benoît, A., Benoit-Lévy, A., Bernard, J. P., Bersanelli, M., Bielewicz, P., Bock, J. J., Bonaldi, A., Bonavera, L., Bond, J. R., Borrill, J., Bouchet, F. R., Boulanger, F., Bucher, M., Burigana, C., Butler, R. C., Calabrese, E., Cardoso, J. F., Casaponsa, B., Catalano, A., Challinor, A., Chamballu, A., Chiang, H. C., Christensen, P. R., Church, S., Clements, D. L., Colombi, S., Colombo, L. P. L., Combet, C., Contreras, D., Couchot, F., Coulais, A., Crill, B. P., Cruz, M., Curto, A., Cuttaia, F., Danese, L., Davies, R. D., Davis, R. J., de Bernardis, P., de Rosa, A., de Zotti, G., Delabrouille, J., Désert, F. X., Diego, J. M., Dole, H., Donzelli, S., Doré, O., Douspis, M., Ducout, A., Dupac, X., Efstathiou, G., Elsner, F., Enßlin, T. A., Eriksen, H. K., Fantaye, Y., Fergusson, J., Fernandez-Cobos, R., Finelli, F., Forni, O., Frailis, M., Fraisse, A. A., Franceschi, E., Frejsel, A., Frolov, A., Galeotta, S., Galli, S., Ganga, K., Gauthier, C., Ghosh, T., Giard, M., Giraud-Héraud, Y., Gjerløw, E., González-Nuevo, J., Górski, K. M., Gratton, S., Gregorio, A., Gruppuso, A., Gudmundsson, J. E., Hansen, F. K., Hanson, D., Harrison, D. L., Henrot-Versillé, S., Hernández-Monteagudo, C., Herranz, D., Hildebrandt, S. R., Hivon, E., Hobson, M., Holmes, W. A., Hornstrup, A., Hovest, W., Huang, Z., Huffenberger, K. M., Hurier, G., Jaffe, A. H., Jaffe, T. R., Jones, W. C., Juvela, M., Keihänen, E., Keskitalo, R., Kim, J., Kisner, T. S., Knoche, J., Kunz, M., Kurki-Suonio, H., Lagache, G., Lähteenmäki, A., Lamarre, J. M., Lasenby, A., Lattanzi, M., Lawrence, C. R., Leonardi, R., Lesgourgues, J., Levrier, F., Liguori, M., Lilje, P. B., Linden-Vørnle, M., Liu, H., López-Caniego, M., Lubin, P. M., Macías-Pérez, J. F., Maggio, G., Maino, D., Mandolesi, N., Mangilli, A., Marinucci, D., Maris, M., Martin, P. G., Martínez-González, E., Masi, S., Matarrese, S., McGehee, P., Meinhold, P. R., Melchiorri, A., Mendes, L., Mennella, A., Migliaccio, M., Mikkelsen, K., Mitra, S., Miville-Deschênes, M. A., Molinari, D., Moneti, A., Montier, L., Morgante, G., Mortlock, D., Moss, A., Munshi, D., Murphy, J. A., Naselsky, P., Nati, F., Natoli, P., Netterfield, C. B., Nørgaard-Nielsen, H. U., Noviello, F., Novikov, D., Novikov, I., Oxborrow, C. A., Paci, F., Pagano, L., Pajot, F., Pant, N., Paoletti,

D., Pasian, F., Patanchon, G., Pearson, T. J., Perdereau, O., Perotto, L., Perrotta, F., Pettorino, V., Piacentini, F., Piat, M., Pierpaoli, E., Pietrobon, D., Plaszczynski, S., Pointecouteau, E., Polenta, G., Popa, L., Pratt, G. W., Prézeau, G., Prunet, S., Puget, J. L., Rachen, J. P., Rebolo, R., Reinecke, M., Remazeilles, M., Renault, C., Renzi, A., Ristorcelli, I., Rocha, G., Rosset, C., Rossetti, M., Rotti, A., Roudier, G., Rubiño-Martín, J. A., Rusholme, B., Sandri, M., Santos, D., Savelainen, M., Savini, G., Scott, D., Seiffert, M. D., Shellard, E. P. S., Souradeep, T., Spencer, L. D., Stolyarov, V., Stompor, R., Sudiwala, R., Sunyaev, R., Sutton, D., Suur-Uski, A. S., Sygnet, J. F., Tauber, J. A., Terenzi, L., Toffolatti, L., Tomasi, M., Tristram, M., Trombetti, T., Tucci, M., Tuovinen, J., Valenziano, L., Valiviita, J., Van Tent, B., Vielva, P., Villa, F., Wade, L. A., Wandelt, B. D., Wehus, I. K., Yvon, D., Zacchei, A., Zibin, J. P., and Zonca, A. (2016). Planck 2015 results. XVI. Isotropy and statistics of the CMB. *A&A*, 594:A16.

Planck Collaboration, Ade, P. A. R., Aghanim, N., Alves, M. I. R., Arnaud, and et al. (2015). Planck intermediate results. XXIII. Galactic plane emission components derived from Planck with ancillary data. *A&A*, 580:A13.

Planck Collaboration, Ade, P. A. R., Aghanim, N., Arnaud, M., Ashdown, M., Atrio-Barandela, F., Aumont, J., Baccigalupi, C., Balbi, A., Banday, A. J., and et al. (2013). Planck intermediate results. VIII. Filaments between interacting clusters. *A&A*, 550:A134.

Pratt, G. W., Arnaud, M., Piffaretti, R., Böhringer, H., Ponman, T. J., Croston, J. H., Voit, G. M., Borgani, S., and Bower, R. G. (2010). Gas entropy in a representative sample of nearby X-ray galaxy clusters (REXCESS): relationship to gas mass fraction. *A&A*, 511:A85.

Randall, S., Nulsen, P., Forman, W. R., Jones, C., Machacek, M., Murray, S. S., and Maughan, B. (2008). Chandra's View of the Ram Pressure Stripped Galaxy M86. *ApJ*, 688:208–223.

Reiprich, T. H., Veronica, A., Pacaud, F., Ramos-Ceja, M. E., Ota, N., Sanders, J., Kara, M., Erben, T., Klein, M., Erler, J., Kerp, J., Hoang, D. N., Brüggen, M., Marvil, J., Rudnick, L., Biffi, V., Dolag, K., Aschersleben, J., Basu, K., Brunner, H., Bulbul, E., Dennerl, K., Eckert, D., Freyberg, M., Gatuzz, E., Ghirardini, V., Käfer, F., Merloni, A., Migkas, K., Nandra, K., Predehl, P., Robrade, J., Salvato, M., Whelan, B., Diaz-Ocampo, A., Hernandez-Lang, D., Zenteno, A., Brown, M. J. I., Collier, J. D., Diego, J. M., Hopkins, A. M., Kapinska, A., Koribalski, B., Mroczkowski, T., Norris, R. P., O'Brien, A., and Vardoulaki, E. (2021). The Abell 3391/95 galaxy cluster system. A 15 Mpc intergalactic medium emission filament, a warm gas bridge, infalling matter clumps, and (re-) accelerated plasma discovered by combining SRG/eROSITA data with ASKAP/EMU and DECam data. *A&A*, 647:A2.

Roediger, E., Kraft, R. P., Nulsen, P. E. J., Forman, W. R., Machacek, M., Randall, S., Jones, C., Churazov, E., and Kokotanekova, R. (2015). Stripped Elliptical Galaxies as Probes of ICM Physics: I. Tails, Wakes, and Flow Patterns in and Around Stripped Ellipticals. *ApJ*, 806:103.

Santos, J. S., Tozzi, P., Rosati, P., and Böhringer, H. (2010). The evolution of cool-core clusters. *A&A*, 521:A64.

Sarkar, A. et al. (2022). A pre-merger shock in the abell 98 system.

Sarkar, A., Su, Y., Randall, S., Gastaldello, F., Trierweiler, I., White, R., Kraft, R., and Miller, E. (2021). Joint Suzaku and Chandra observations of the MKW4 galaxy group out to the virial radius. *MNRAS*, 501(3):3767–3780.

Schellenberger, G. and Reiprich, T. H. (2017). HICOSMO: cosmology with a complete sample of galaxy clusters - II. Cosmological results. *MNRAS*, 471(2):1370–1389.

Schellenberger, G., Reiprich, T. H., Lovisari, L., Nevalainen, J., and David, L. (2015). XMM-Newton and Chandra cross-calibration using HIFLUGCS galaxy clusters . Systematic temperature differences and cosmological impact. *A&A*, 575:A30.

Schneider, P. and Seitz, C. (1995). Steps towards nonlinear cluster inversion through gravitational distortions. I. Basic considerations and circular clusters. *A&A*, 294:411–431.

Simionescu, A., Allen, S. W., Mantz, A., Werner, N., Takei, Y., Morris, R. G., Fabian, A. C., Sanders, J. S., Nulsen, P. E. J., George, M. R., and Taylor, G. B. (2011). Baryons at the Edge of the X-ray-Brightest Galaxy Cluster. *Science*, 331:1576.

Sinha, M. and Holley-Bockelmann, K. (2010). Balancing the baryon budget: the fraction of the IGM due to galaxy mergers. *MNRAS*, 405:L31–L35.

Smith, R. K., Brickhouse, N. S., Liedahl, D. A., and Raymond, J. C. (2001). Collisional Plasma Models with APEC/APED: Emission-Line Diagnostics of Hydrogen-like and Helium-like Ions. *ApJl*, 556:L91–L95.

Starck, J. L., Donoho, D. L., and Candès, E. J. (2003). Astronomical image representation by the curvelet transform. *A&A*, 398:785–800.

Struble, M. F. and Rood, H. J. (1999). A Compilation of Redshifts and Velocity Dispersions for ACO Clusters. *ApJs*, 125:35–71.

Su, Y., Buote, D., Gastaldello, F., and Brighenti, F. (2015). The Entire Virial Radius of the Fossil Cluster RX J1159+5531: I. Gas Properties. *ApJ*, 805:104.

Sugawara, Y., Takizawa, M., Itahana, M., Akamatsu, H., Fujita, Y., Ohashi, T., and Ishisaki, Y. (2017). Suzaku Observations of the Outskirts of the Galaxy Cluster Abell 3395 including a Filament toward Abell 3391. *ArXiv e-prints*.

Sun, M., Voit, G. M., Donahue, M., Jones, C., Forman, W., and Vikhlinin, A. (2009). Chandra Studies of the X-Ray Gas Properties of Galaxy Groups. *ApJ*, 693:1142–1172.

Sunyaev, R. A. and Zeldovich, I. B. (1980). Microwave background radiation as a probe of the contemporary structure and history of the universe. *ARA&A*, 18:537–560.

Sunyaev, R. A. and Zeldovich, Y. B. (1970). Small-Scale Fluctuations of Relic Radiation. *Ap&SS*, 7(1):3–19.

Tawa, N., Hayashida, K., Nagai, M., Nakamoto, H., Tsunemi, H., Yamaguchi, H., Ishisaki, Y., Miller, E. D., Mizuno, T., Dotani, T., Ozaki, M., and Katayama, H. (2008). Reproducibility of Non-X-Ray Background for the X-Ray Imaging Spectrometer aboard Suzaku. *PASJ*, 60:S11–S24.

Tchernin, C., Eckert, D., Ettori, S., Pointecouteau, E., Paltani, S., Molendi, S., Hurier, G., Gastaldello, F., Lau, E. T., Nagai, D., Roncarelli, M., and Rossetti, M. (2016). The XMM Cluster Outskirts Project (X-COP): Physical conditions of Abell 2142 up to the virial radius. *A&A*, 595:A42.

Tittley, E. R. and Henriksen, M. (2001). A Filament between Galaxy Clusters A3391 and A3395. *ApJ*, 563:673–686.

Tritton, K. P. (1972). New redshifts of radio galaxies. *MNRAS*, 158:277–280.

Urban, O., Simionescu, A., Werner, N., Allen, S. W., Ehlert, S., Zhuravleva, I., Morris, R. G., Fabian, A. C., Mantz, A., Nulsen, P. E. J., Sanders, J. S., and Takei, Y. (2014). Azimuthally resolved X-ray spectroscopy to the edge of the Perseus Cluster. *MNRAS*, 437:3939–3961.

Valageas, P., Schaeffer, R., and Silk, J. (2003). The phase diagram of the intergalactic medium and the entropy floor of groups and clusters: are clusters born warm? *MNRAS*, 344:53–59.

Vazza, F., Brunetti, G., Kritsuk, A., Wagner, R., Gheller, C., and Norman, M. (2009). Turbulent motions and shocks waves in galaxy clusters simulated with adaptive mesh refinement. *A&A*, 504:33–43.

Vikhlinin, A., Burenin, R. A., Ebeling, H., Forman, W. R., Hornstrup, A., Jones, C., Kravtsov, A. V., Murray, S. S., Nagai, D., Quintana, H., and Voevodkin, A. (2009). Chandra Cluster Cosmology Project. II. Samples and X-Ray Data Reduction. *ApJ*, 692:1033–1059.

Voit, G. M., Kay, S. T., and Bryan, G. L. (2005). The baseline intracluster entropy profile from gravitational structure formation. *MNRAS*, 364:909–916.

Walker, S. A., Fabian, A. C., Sanders, J. S., George, M. R., and Tawara, Y. (2012). X-ray observations of the galaxy cluster Abell 2029 to the virial radius. *MNRAS*, 422:3503–3515.

Walker, S. A., Fabian, A. C., Sanders, J. S., Simionescu, A., and Tawara, Y. (2013). X-ray exploration of the outskirts of the nearby Centaurus cluster using Suzaku and Chandra. *MNRAS*, 432:554–569.

Wang, Q. D., Connolly, A. J., and Brunner, R. J. (1997). A2125 and Its Environs: Evidence for an X-Ray-Emitting Hierarchical Superstructure. *ApJl*, 487:L13–L16.

Werner, N., Finoguenov, A., Kaastra, J. S., Simionescu, A., Dietrich, J. P., Vink, J., and Böhringer, H. (2008). Detection of hot gas in the filament connecting the clusters of galaxies Abell 222 and Abell 223. *A&A*, 482:L29–L33.

White, D. A., Jones, C., and Forman, W. (1997). An investigation of cooling flows and general cluster properties from an X-ray image deprojection analysis of 207 clusters of galaxies. *MNRAS*, 292(2):419–467.

Wong, K.-W. and Sarazin, C. L. (2009). Effects of the Non-Equipartition of Electrons and Ions in the Outskirts of Relaxed Galaxy Clusters. *ApJ*, 707:1141–1159.

Zappacosta, L., Nicastro, F., Krongold, Y., and Maiolino, R. (2012). An X-Ray WHIM Metal Absorber from a Mpc-scale Empty Region of Space. *ApJ*, 753:137.

Zhang, B., Fadili, J. M., and Starck, J.-L. (2008). Wavelets, Ridgelets, and Curvelets for Poisson Noise Removal. *IEEE Transactions on Image Processing*, 17:1093–1108.